An update to this article is included at the end

Article

Cancer Cell

KDM5 Histone Demethylase Activity Links Cellular Transcriptomic Heterogeneity to Therapeutic Resistance

Graphical Abstract

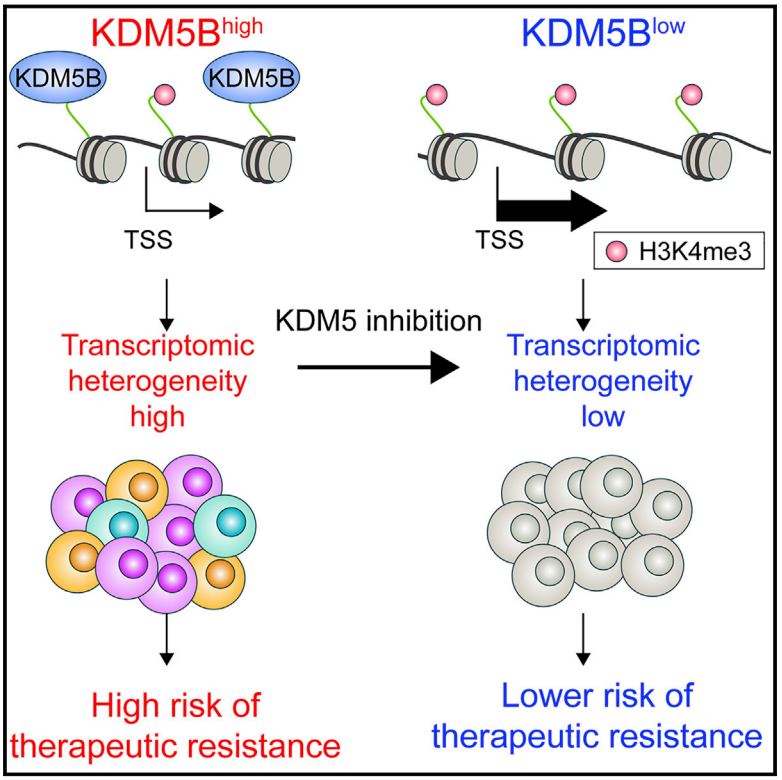

Highlights

- KDM5 activity modulates response and resistance to endocrine therapies
- Endocrine resistance is due to selection for pre-existing distinct cell populations
- Acquired KDM5 inhibitor resistance is epigenetic, including gain of ER signaling
- Transcriptomic but not genetic heterogeneity is associated with higher KDM5B

Authors

Kunihiko Hinohara, Hua-Jun Wu, Sébastien Vigneau, ..., Alexander A. Gimelbrant, Franziska Michor, Kornelia Polyak

Correspondence

michor@jimmy.harvard.edu (F.M.), kornelia_polyak@dfci.harvard.edu (K.P.)

In Brief

Hinohara et al. demonstrate that histone demethylases KDM5A and KDM5B are key regulators of phenotypic heterogeneity in estrogen receptor (ER)-positive breast cancer. Inhibition of KDM5 activity increases sensitivity to endocrine therapy by modulating ER signaling.

Hinohara et al., 2018, Cancer Cell *34*, 939–953
December 10, 2018
https://doi.org/10.1016/j.ccell.2018.10.014

CellPress

Cancer Cell
Article

KDM5 Histone Demethylase Activity Links Cellular Transcriptomic Heterogeneity to Therapeutic Resistance

Kunihiko Hinohara,[1,2,16] Hua-Jun Wu,[3,4,5,16] Sébastien Vigneau,[6,7] Thomas O. McDonald,[3,4,5,8] Kyomi J. Igarashi,[6,7,13] Kimiyo N. Yamamoto,[3,4,5] Thomas Madsen,[3,4,5] Anne Fassl,[6,7] Shawn B. Egri,[9] Malvina Papanastasiou,[9] Lina Ding,[1,2] Guillermo Peluffo,[1,2] Ofir Cohen,[1,9] Stephen C. Kales,[10] Madhu Lal-Nag,[10] Ganesha Rai,[10] David J. Maloney,[10,14] Ajit Jadhav,[10] Anton Simeonov,[10] Nikhil Wagle,[1,2,9] Myles Brown,[1,2,11,12] Alexander Meissner,[5,9,15] Piotr Sicinski,[6,7] Jacob D. Jaffe,[9] Rinath Jeselsohn,[1,2] Alexander A. Gimelbrant,[6,7] Franziska Michor,[3,4,5,8,9,12,*] and Kornelia Polyak[1,2,8,9,11,12,17,*]

[1]Department of Medical Oncology, Dana-Farber Cancer Institute, Boston, MA 02215, USA
[2]Department of Medicine, Harvard Medical School, Boston, MA 02115, USA
[3]Department of Biostatistics and Computational Biology, Dana-Farber Cancer Institute, Boston, MA 02215, USA
[4]Department of Biostatistics, Harvard T. H. Chan School of Public Health, Boston, MA 02115, USA
[5]Department of Stem Cell and Regenerative Biology, Harvard University, Cambridge, MA 02138, USA
[6]Department of Cancer Biology, Dana-Farber Cancer Institute, Boston, MA 02215, USA
[7]Department of Genetics, Harvard Medical School, Boston, MA 02115, USA
[8]Center for Cancer Evolution, Dana-Farber Cancer Institute, Boston, MA 02215, USA
[9]The Eli and Edythe L Broad Institute of MIT and Harvard, Cambridge, MA 02139, USA
[10]National Center for Advancing Translational Sciences, Bethesda, MD 20892, USA
[11]Center for Functional Cancer Epigenetics, Dana-Farber Cancer Institute, Boston, MA 02215, USA
[12]Ludwig Center at Harvard, Boston, MA 02215, USA
[13]Present address: Stanford University School of Medicine, Stanford, CA 94305, USA
[14]Present address: Inspyr Therapeutics, 31200 Via Colinas, Suite 200, Westlake Village, CA 91362, USA
[15]Present address: Department of Genome Regulation, Max Planck Institute for Molecular Genetics, Berlin 14195, Germany
[16]These authors contributed equally
[17]Lead Contact
*Correspondence: michor@jimmy.harvard.edu (F.M.), kornelia_polyak@dfci.harvard.edu (K.P.)
https://doi.org/10.1016/j.ccell.2018.10.014

SUMMARY

Members of the KDM5 histone H3 lysine 4 demethylase family are associated with therapeutic resistance, including endocrine resistance in breast cancer, but the underlying mechanism is poorly defined. Here we show that genetic deletion of *KDM5A/B* or inhibition of KDM5 activity increases sensitivity to anti-estrogens by modulating estrogen receptor (ER) signaling and by decreasing cellular transcriptomic heterogeneity. Higher *KDM5B* expression levels are associated with higher transcriptomic heterogeneity and poor prognosis in ER^+ breast tumors. Single-cell RNA sequencing, cellular barcoding, and mathematical modeling demonstrate that endocrine resistance is due to selection for pre-existing genetically distinct cells, while KDM5 inhibitor resistance is acquired. Our findings highlight the importance of cellular phenotypic heterogeneity in therapeutic resistance and identify KDM5A/B as key regulators of this process.

Significance

Cellular heterogeneity for phenotypic features is a key mechanism underlying disease progression and therapeutic resistance, yet its regulation is poorly understood at the molecular level. Our findings demonstrate that endocrine resistance is associated with higher transcriptomic heterogeneity and provide proof of principle for how decreasing cellular transcriptomic heterogeneity by modulating the activity of epigenetic enzymes, such as KDM5 family members, can lead to improved responses to treatment. We also present conclusive evidence that acquired resistance to anti-estrogens and KDM5 inhibitors is mechanistically distinct; although both involve gain of estrogen-independent growth. These observations suggest that epigenetic agents may improve the efficacy of cancer therapies when used in combination, even when they have limited activity as single agents.

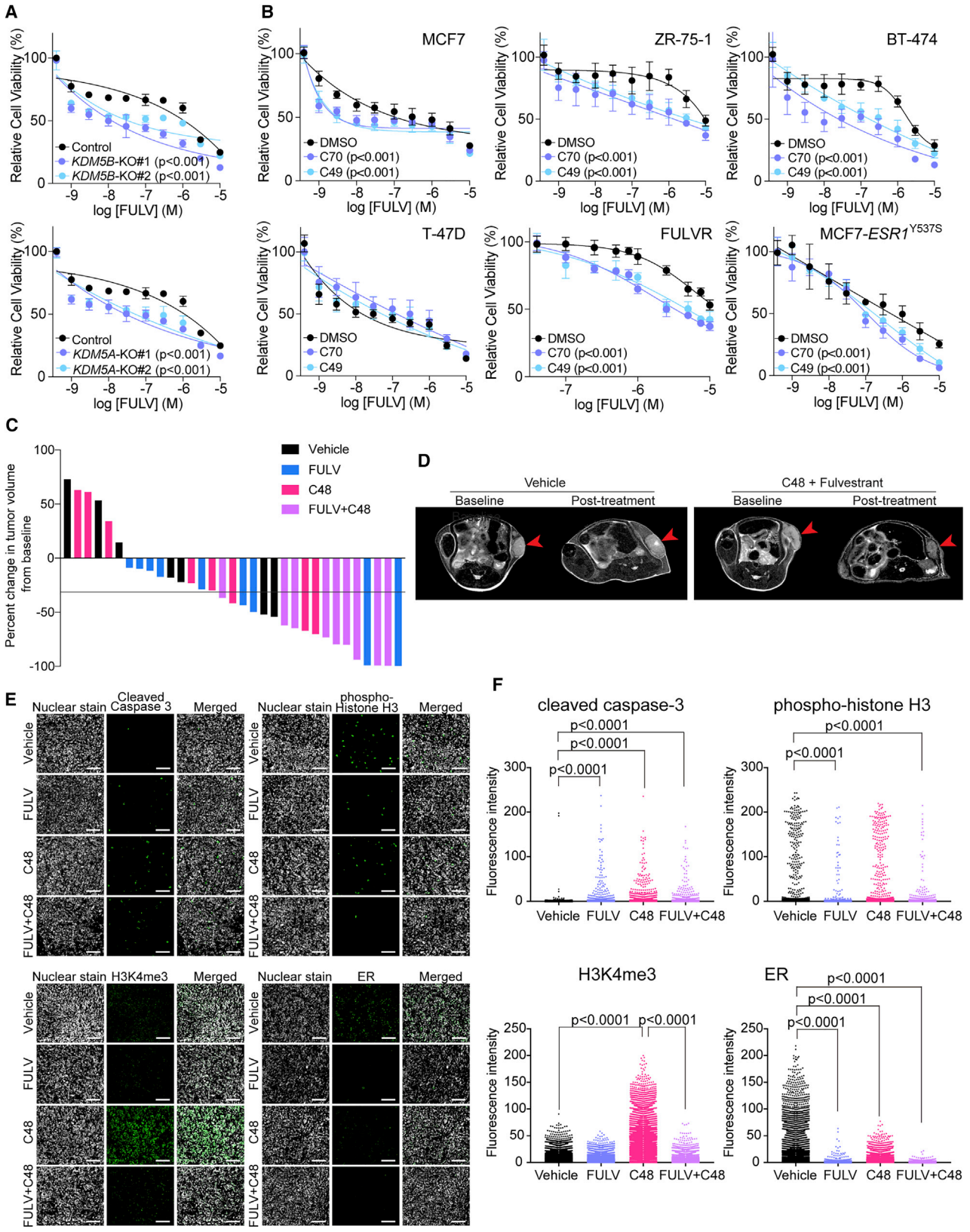

(legend on next page)

INTRODUCTION

Modulation of chromatin structure due to post-translational modification of histones plays a key role in establishing cell-type-specific gene expression patterns, and alterations of this process are involved in tumorigenesis (Flavahan et al., 2017). Frequent mutations of genes encoding for chromatin-modifying enzymes and histones in multiple human cancer types further emphasize the role of perturbed epigenetic programs in tumor evolution (Feinberg et al., 2016). However, the functional consequences of these mutations remain relatively poorly characterized.

In breast cancer, epigenetic regulators and transcription factors are among the most frequently mutated genes, especially in luminal tumors (Cancer Genome Atlas Network, 2012). More recent sequencing of endocrine-resistant metastatic breast tumors has identified alterations previously not detected in primary tumors, such as *ESR1* mutations in a subset of cases (Jeselsohn et al., 2015). Most of these *ESR1* mutations occur in the ligand-binding domain (e.g., *ESR1*^{Y537S}) and confer decreased sensitivity to anti-estrogens such as fulvestrant and tamoxifen. The majority (~70%) of breast cancer patients are diagnosed with estrogen receptor-positive (ER$^+$) hormone-dependent tumors and many progress to treatment-resistant metastatic disease. Therefore, a better understanding of the mechanisms of endocrine resistance and identification of strategies to decrease or prevent it would have high clinical impact.

We previously reported that *KDM5B*, encoding a histone H3 lysine 4 (H3K4) demethylase, is an oncogene in luminal ER$^+$ breast cancer due to its frequent amplification and overexpression, and its higher activity being associated with shorter disease-free survival in breast cancer patients treated with endocrine therapy (Yamamoto et al., 2014). *KDM5B* was also identified as a gene required for tumor maintenance in melanoma (Roesch et al., 2010), and its increased expression is associated with resistance to BRAF inhibitors and chemotherapy (Roesch et al., 2013). Other KDM5 family members such as *KDM5A* have also been implicated in therapeutic resistance in lung and other cancer types (Sharma et al., 2010), triggering an interest in developing KDM5 inhibitors (KDM5i) for cancer treatment (Horton et al., 2016; Johansson et al., 2016; Vinogradova et al., 2016). However, the mechanisms by which the KDM5 family of histone demethylases (HDMs) contribute to tumorigenesis and therapy resistance remains poorly defined.

RESULTS

The Effect of KDM5B and KDM5A on Sensitivity to Endocrine Therapies

To explore the function of KDM5B and KDM5A in response and resistance to endocrine therapies in breast cancer, we deleted *KDM5B* and *KDM5A* in the MCF7 ER$^+$ estrogen-dependent luminal breast cancer cell line using CRISPR-Cas9. Both *KDM5B*-knockout (KO) and *KDM5A*-KO cells demonstrated increased sensitivity to fulvestrant compared with parental MCF7 cells (Figure 1A). *KDM5B*-KO cells and *KDM5A*-KO cells also showed decreased cell proliferation (Figure S1A) and increased H3K4me3 levels (Figure S1B) at early passage; however, at later passages these phenotypic differences disappeared (Figure S1A) likely due to selection for cells that can compensate for the loss. Hence, to be able to inhibit all KDM5 activity in a dynamic manner, we utilized two recently developed small-molecule inhibitors of the KDM5 family of enzymes KDM5-C49 (C49) and its cell-permeable ethyl ester derivative KDM5-C70 (C70) (Johansson et al., 2016) to further characterize the link between KDM5 activity and endocrine therapies.

We confirmed the specificity of these inhibitors by mass spectrometry analysis of histone modifications (Creech et al., 2015) and by testing their effects on *KDM5A/B*-KO cells. We found that among all histone modifications analyzed, only H3K4me3 showed a significant increase after C70 and C49 treatment (Figure S1C). Similarly, while both KDM5i effectively decreased the growth of parental MCF7 cells, deletion of *KDM5B* or *KDM5A* diminished this effect (Figures S1D and S1E). These results imply that KDM5B and KDM5A are key mediators of KDM5i-mediated growth suppression in these cells. Immunoblot analysis also demonstrated increased H3K4me3 levels after KDM5i treatment in parental MCF7 but not in *KDM5B*-KO cells (Figure S1F). In line with our previous studies demonstrating that KDM5B is more relevant in luminal breast cancer cells (Yamamoto et al., 2014), we confirmed higher *KDM5B* expression levels in luminal compared with basal-like breast cancer cells (Figures S1G and S1H) and that ER$^+$ primary tumors with higher *KDM5B* expression levels were more likely to develop local and distant metastatic recurrence in tamoxifen-treated breast cancer patients (Figure S1I). We also observed significant growth inhibition in luminal but not in non-luminal breast cancer cell lines following KDM5i treatment, even though increased H3K4me3 was detected in all lines tested (Figures S1J and S1K). Gene expression profiling of MCF7 cells at different time points following C70 treatment demonstrated progressive gene expression changes (Table S1) and upregulated genes showed enrichment in transforming growth factor β signaling (Figure S1L), which is in agreement with our prior data using siKDM5B (Yamamoto et al., 2014). Based on these experiments, we conclude that C49 and C70 appear to mimic the loss of *KDM5B* or *KDM5A* in breast cancer cells.

To investigate whether decreasing KDM5 activity would enhance sensitivity to endocrine therapies, we pre-treated ER$^+$ breast cancer cell lines (MCF7, ZR-75-1, BT-474, and T-47D), fulvestrant-resistant (FULVR), and *ESR1*^{Y537S} mutant-expressing

Figure 1. The Role of KDM5B and KDM5A in Endocrine Therapies

(A) Cellular viability after fulvestrant treatment of parental MCF7, *KDM5B*-KO, and *KDM5A*-KO cells.

(B) Cellular viability after fulvestrant treatment of a panel of breast cancer cell lines pre-treated with DMSO or KDM5i.

(C) Graph depicting percent change in tumor volume from baseline in control, fulvestrant (FULV), C48, and combined treatment groups. Black line marks 30% decrease in volume, which is commonly used as a cutoff to define response in clinical studies.

(D) Representative MRI images of tumors before and after treatment in vehicle and combined C48 + FULV group.

(E) Representative immunofluorescence analysis of the indicated markers in tumors of the four treatment groups. Scale bars, 100 μm.

(F) Graphs depicting quantification of immunofluorescence images.

In (A) and (B), Error bars represent SD, n = 6. See also Figure S1 and Table S1.

derivatives with KDM5i followed by combined treatment with fulvestrant. We found that inhibition of KDM5 increased cellular sensitivity to fulvestrant in all cell lines tested except in T-47D cells (Figure 1B). To validate these findings *in vivo*, we performed xenograft assays using MCF7 cells and C48, a KDM5i suitable for *in vivo* use (Liang et al., 2016). We first confirmed that C48 also increased cellular sensitivity to fulvestrant in cell culture (Figure S1M). Next, we treated pre-established MCF7 xenografts with fulvestrant, C48, and their combination. Combined treatment led to a significant decrease in tumor volume, while neither compound by itself had the same effect (Figures 1C and 1D). Tumor histology was not affected by any of the treatments based on analysis of H&E-stained slides (Figure S1N). However, assessment of cell proliferation and apoptosis by immunofluorescence for phospho-histone H3 and cleaved caspase-3, respectively, demonstrated a significant increase in apoptosis in all treatment groups and decreased proliferation after fulvestrant and combined treatment (Figures 1E and 1F). Immunofluorescence for H3K4me3 and ER also confirmed significantly increased H3K4me3 after C48 and decreased ER after fulvestrant treatment (Figures 1E and 1F), which we also confirmed in cell culture and by immunoblot (Figures S1O and S1P). These findings suggest that KDM5 HDMs regulate sensitivity to endocrine therapy in both hormone-sensitive and endocrine-resistant cells both *in vitro* and *in vivo*.

KDM5 Activity, H3K4me3 Broadness, and Variability in Gene Expression

Recent studies have shown that genes marked by the broadest H3K4me3 promoter domains exhibit enhanced transcriptional consistency (Benayoun et al., 2014), implying that regulators of H3K4me3 peak broadness, such as KDM5, may regulate cellular transcriptomic heterogeneity. To test this hypothesis, we investigated changes in H3K4me3 chromatin patterns following KDM5 inhibition by performing chromatin immunoprecipitation sequencing (ChIP-seq) for H3K4me3 and H3K4me2 in a panel of breast cancer cell lines. Because our prior data demonstrated that KDM5B histone demethylase activity may be modulated by CTCF (higher HDM activity at KDM5B-CTCF overlapping peaks) (Yamamoto et al., 2014), we also performed ChIP-seq for CTCF. C70 treatment globally increased the broadness of promoter H3K4me3 peaks over time without increasing peak height, while H3K4me2 peak heights were slightly decreased (Figures 2A and S2A). Increased H3K4me3 peak broadness was also confirmed in both *KDM5B*-KO and *KDM5A*-KO cells (Figure S2B). The correlation between promoter H3K4me3 peak width and transcript levels remained constant during C70 treatment (Figure S2C), although an increase in broadness led to an increase in gene expression (Figure S2D). The increase in H3K4me3 peak broadness was significantly higher at KDM5B-CTCF overlapping versus non-overlapping sites (Figure S2E) in line with our previous findings demonstrating significant differences in H3K4me3 levels between KDM5B-CTCF overlapping versus non-overlapping sites (Yamamoto et al., 2014). The top 500 genes with H3K4me3 peak broadness increase were also associated with enriched binding of transcriptional elongation mark H3K79me2 after C70 treatment (Figure S2F), implying that changes in H3K4me3 peak broadness may influence transcriptional elongation. At loci with the most significant increase in H3K4me3 peak broadness, such as in *ZMYND8* encoding for a KDM5D corepressor (Li et al., 2016), KDM5B and H3K4me3 peaks showed a clear overlap, suggesting that the decrease in KDM5B activity is directly linked to increased H3K4me3 broadness (Figure 2B).

To assess whether these dynamic changes in H3K4me3 peak broadness alter cell-to-cell variability in gene expression, we performed inDrop single-cell RNA sequencing (scRNA-seq) (Zilionis et al., 2017) to characterize the expression profiles of 500–2,000 individual cells in parental and C70-treated cells. We found that an increase in H3K4me3 broadness was significantly associated with an increase in the fraction of cells expressing the associated genes, with *ZMYND8* being the top upregulated gene (Figures 2C and 2D). Limiting the analysis to genes without expression changes in bulk samples provided similar results (Figure 2C), thus excluding the bias from changes in gene expression on fraction of expressing cells. These results suggest that changes in H3K4me3 peak broadness following KDM5 inhibition lead to more uniform cellular gene expression patterns.

KDM5 Activity and Cellular Transcriptomic Heterogeneity

Cellular heterogeneity of phenotypic features is a key mechanism underlying disease progression and therapeutic resistance (Huang, 2013), yet its regulation at the molecular level is poorly understood. We hypothesized that modulating KDM5 activity might affect cell-to-cell transcriptomic heterogeneity and impact therapeutic resistance via this mechanism. To test this hypothesis, we analyzed scRNA-seq data of breast cancer cell lines before and after treatment with C70 or FULV (Figure S3A), and investigated the cell-to-cell variability for the expression of selected genes using the Gini coefficient (Jiang et al., 2016), where a higher Gini coefficient value indicates more heterogeneous expression. We also generated and analyzed derivatives of MCF7 cells that acquired resistance to C70 during prolonged culture (C70R) to gain insights into the relationship between acquired resistance to KDM5i and cellular transcriptomic heterogeneity. The majority of genes detected had a relatively high Gini index (Figure 3A), suggesting that most genes were expressed heterogeneously, although confounding due to technical issues of scRNA-seq cannot be excluded. Thus, we also performed CyTOF using a panel of markers corresponding to cellular states and activity of signaling pathways and confirmed that the Gini indices calculated based on inDrop and CyTOF data were correlated (Figure S3B). The Gini indices of both *KDM5B* and *KDM5A* were >0.5, suggesting relatively heterogeneous expression of these genes (Figures 3A and S3C). Consistent with the increase in the fraction of cells expressing *ZMYND8* after C70 treatment, *ZMYND8* had a lower Gini index in C70-treated cells compared with untreated control (Figures 3A and 3B). The Gini indices of luminal lineage-specific genes (e.g., *GATA3* and *FOXA1*) were <0.5 in luminal but >0.9 in mesenchymal SUM159 cells, while mesenchymal-lineage-specific genes (e.g., VIM) showed the opposite pattern (Figures 3A and S3C). The observed differences are not likely to be due to differences in cell proliferation as there was no significant difference in the distribution of cells in different phases of cell cycle among samples (Figure S3D).

To assess the effects of KDM5 activity on cellular transcriptomic heterogeneity, we determined the cell-to-cell distance

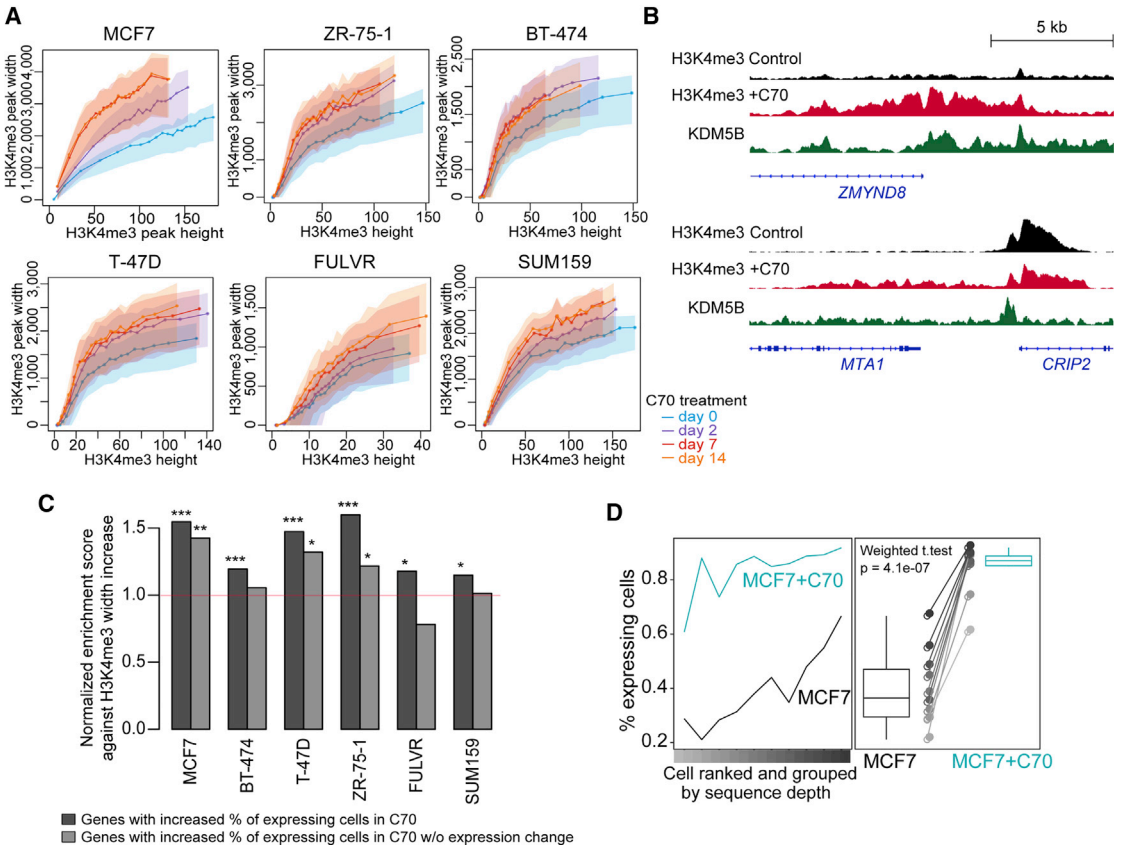

Figure 2. H3K4me3 Peak Broadness and Transcriptomic Variability

(A) H3K4me3 and H3K4me2 peak width plotted against peak height before and at different time points (day 0–14) after treatment with C70 inhibitor. Mean values are shown as dotted lines. Shaded areas indicate interquartile range (IQR).

(B) Gene tracks depicting KDM5B and H3K4me3 signal at selected genomic loci. The x axis shows position along the chromosome with gene structures drawn below, whereas the y axis shows genomic occupancy in units of reads per million reads (RPM).

(C) Correlation between promoter H3K4me3 peak broadness changes and changes in percent of cells expressing the corresponding gene in C70-treated cells. Enrichment analysis of H3K4me3 width increase in C70 is performed against the genes with increased percent of expressing cells in C70 for all genes or genes without expression change. H3K4me3 width changes are calculated as the average width changes across all six cell lines. ***False discovery rate (FDR) < 0.001; **FDR < 0.01; *FDR < 0.25.

(D) Plot depicting percentage of cells expressing *ZMYND8* in MCF7 and C70-treated MCF7 cells. All single cells are ranked and grouped into ten groups based on their sequence depth to avoid variability due to this. The percent of expressing cells is calculated for each group, and a weighted t test is performed to access the significance of the difference between two samples. The box indicates the IQR, the line inside the box shows the median and whiskers show the locations of either 1.5 × IQR above the third quartile or 1.5 × IQR below the first quartile. See also Figure S2.

among cells based on scRNA-seq data. Interestingly, KDM5i treatment decreased cell-to-cell transcriptomic heterogeneity of luminal ER$^+$ breast cancer cells, with the exception of T-47D cells, and increased it in the SUM159 mesenchymal cell line (Figure 3C). In contrast to short-term C70-treated cells, the cell-to-cell transcriptomic heterogeneity of KDM5i-resistant C70R cells was similar to parental MCF7 cells. Fulvestrant-treated MCF7 cells had higher heterogeneity than parental MCF7 cells and this was further increased in the FULVR population, but decreased after KDM5i treatment (Figure 3C). Analysis of changes in the Gini index also demonstrated a decrease for the majority of genes after C70 treatment in luminal ER$^+$, but not in the SUM159 mesenchymal breast cancer cell line, further suggesting that KDM5 inhibition decreases transcriptomic heterogeneity especially in hormone-sensitive and endocrine-resistant cells (Figure 3D). The observation that C70 treatment does not decrease cellular transcriptomic heterogeneity in T-47D cells (Figure 3C), and does not sensitize these cells to fulvestrant (Figure 1B), further supports our hypothesis that KDM5 inhibition decreases therapeutic resistance by decreasing cell population heterogeneity. Metacore analysis of genes with a decreased Gini index after C70 treatment demonstrated enrichment for proliferation and survival-related pathways including insulin growth factor and ESR1/AP-1 signaling (Figure 3E), which may contribute to the enhanced responsiveness of C70-treated cells to fulvestrant. These results provide strong experimental data to support our hypothesis that KDM5 HDMs are key regulators of cellular transcriptomic heterogeneity and can decrease therapeutic resistance via this function. Furthermore, they also demonstrate that endocrine resistance is associated with increased cellular transcriptomic heterogeneity.

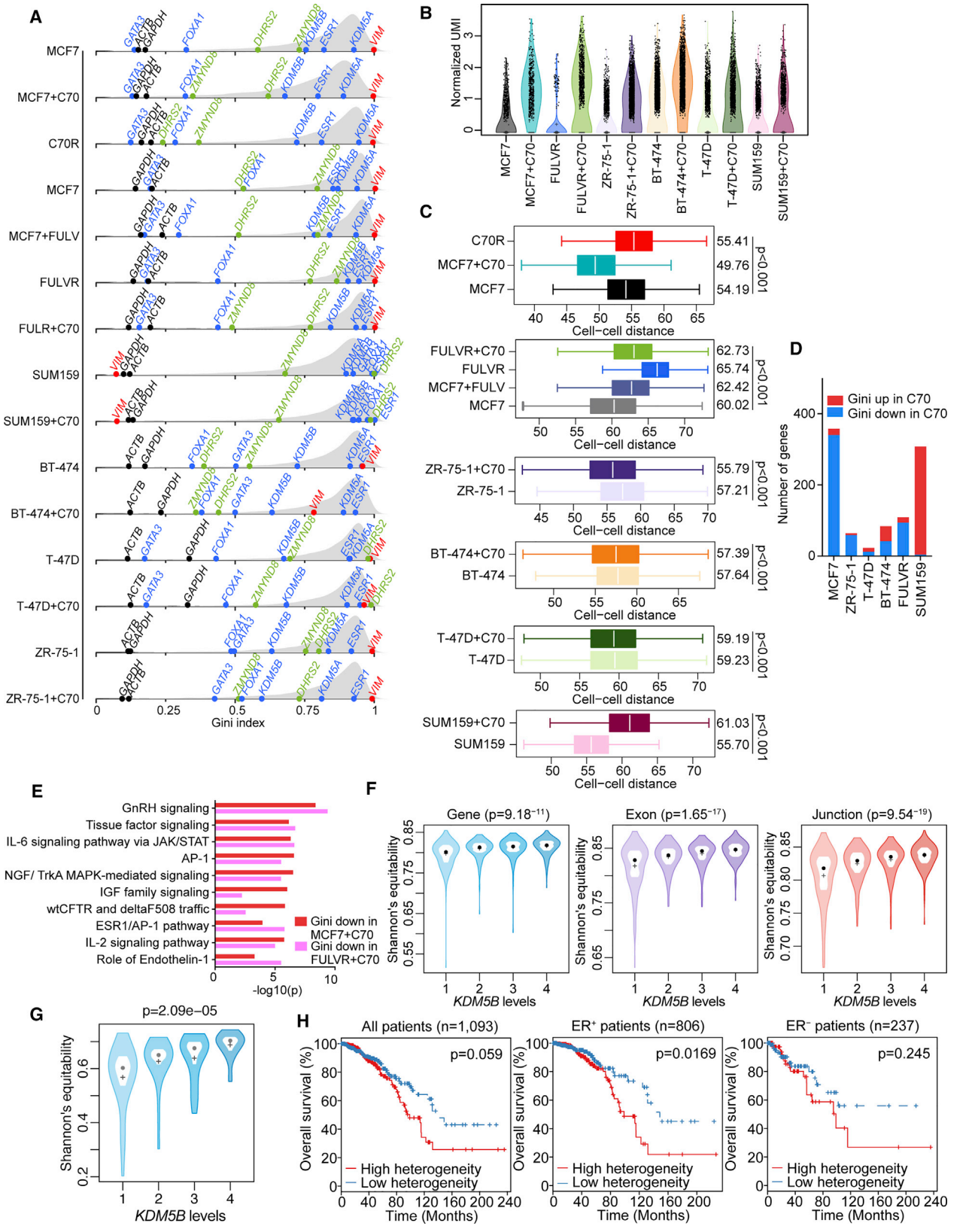

(legend on next page)

To validate these findings in human primary breast tumor samples, we calculated the Shannon's equitability of transcriptomic heterogeneity of breast tumors in three different ways (based on the gene, exon, and exon-junction levels) in the TCGA breast cancer patient cohort (Cancer Genome Atlas Network, 2012) and analyzed potential associations of the extent of heterogeneity with *KDM5B* mRNA levels. The *KDM5B* mRNA level showed a statistically significant association with Shannon's equitability when analyzing all or only ER^+ breast tumors, but this association was not or much less significant in ER^- tumors depending on how transcriptional heterogeneity was calculated (Figures 3F and S3E). *KDM5B* mRNA levels also showed significant association with Shannon's equitability in treatment-resistant distant metastases of ER^+ breast cancer (Figure 3G), implying that KDM5B may play a role in both disease progression and therapy resistance. To assess if this observation is unique to *KDM5B*, we also analyzed possible associations between transcriptomic heterogeneity and the expression of each of the 18 known HDMs and 12 housekeeping genes in the TCGA data (Figure S3F). We found that higher expressions of multiple histone demethylases correlated with higher transcriptomic heterogeneity, but only *KDM5B*, *KDM5C*, and *KDM6B*, showed significant correlation only in luminal ER^+ but not in ER^- breast tumors. In contrast, housekeeping genes showed the opposite pattern and their lower expression was correlated with higher transcriptomic heterogeneity. These data imply that histone demethylases in general may play a role in regulating transcriptomic heterogeneity within tumors, but only *KDM5B*, *KDM5C*, and *KDM6B* are specific mediators of this heterogeneity in ER^+ breast cancers.

To investigate if transcriptomic heterogeneity is simply a reflection of genetic heterogeneity, we also analyzed associations between subclonal mutation fraction and *KDM5B* mRNA levels in the TCGA cohort. *KDM5B* mRNA levels were negatively correlated with subclonal mutation fraction in ER^- tumors but it was not significant in ER^+ tumors (Figure S3G). Similarly, the percent of subclonal mutations in KDM5i- and endocrine-resistant MCF7 cells did not correlate with transcriptomic heterogeneity (Figure S3H). To investigate the clinical relevance of transcriptomic heterogeneity in breast cancer, we analyzed molecular data from 1,093 invasive breast carcinomas in the TCGA. Patients with high transcriptomic heterogeneity ER^+ tumors had shorter overall survival than patients with low transcriptomic heterogeneity tumors (Figure 3H). High transcriptomic heterogeneity had a hazard ratio of 1.85 (95% confidence interval: 1.11–3.08, p = 0.0169) in ER^+ tumors compared with low transcriptomic heterogeneity. Thus, our results suggest that cellular phenotypic but not genetic heterogeneity may underlie resistance to endocrine therapies in ER^+ breast tumors and that this trait is regulated by KDM5 HDM activity.

Mechanism of Acquired KDM5i Resistance

KDM5i are potential therapeutic agents in breast and other cancer types (Johansson et al., 2016). However, inherent or acquired resistance to targeted therapies inevitably occurs during cancer treatment (Gerlinger et al., 2014). Characterizing mechanisms of resistance can aid in the identification of key downstream targets of drugs that mediate their tumor-suppressive effects. Thus, we generated and analyzed derivatives of MCF7 cells that acquired resistance to C70 (C70R) and C49 (C49R) during prolonged culture. The half maximal inhibitory concentration (IC_{50}) of KDM5i-resistant (KDM5IR) cells significantly increased compared with the parental line, and each cell line was resistant to both KDM5i (Figure 4A) and displayed morphology changes characterized by tighter epithelial clusters (Figure 4B). Consistent with this enhanced epithelial morphology, gene expression profiling demonstrated a decrease in EMT-related genes (Figure S4A; Table S2). C70R and C49R cells showed largely overlapping gene expression differences compared with parental MCF7 cells (Figure S4B), which was also reflected in the commonality of signaling pathways enriched in differentially expressed genes (Figure S4A). Interestingly, the top 500 genes upregulated in C70R compared with MCF7 cells showed enrichment in genes highly expressed in FULVR and tamoxifen-resistant (TAMR) cells, while the opposite was observed for downregulated genes (Figure 4C; Table S3), implying that resistance to endocrine therapies and KDM5i may have common underlying mechanisms. Indeed, FULVR-, TAMR-, and $ESR1^{Y537S}$-expressing MCF7 cells were also more resistant to KDM5i than parental MCF7 cells (Figure 4D), although KDM5IR cells retained sensitivity to endocrine therapies (Figure S4C).

Figure 3. KDM5 Activity and Transcriptomic Heterogeneity

(A) Gini index of single-cell inDrop data. The distribution of Gini coefficients of all genes in each sample is shown as a gray density plot. Selected luminal (blue), basal/mesenchymal (red), KDM5i-induced (green), and housekeeping (black) genes are highlighted.

(B) Violin plot showing distribution of normalized expression of *ZMYND8* based on scRNA-seq data. Dots within violin represent the transcript counts in single cells. The "–" and "+" inside the violin indicate the median and mean values, respectively.

(C) Graphs depicting cell-to-cell distance in the indicated cell populations. Wilcoxon rank-sum test p values are shown. Note the analysis of pairwise distances between all single cells generates a large number of data points, which makes the p value less informative than the relative differences between mean values (shown on the right side) and box profiles. The box indicates the IQR, the line inside the box shows the median, and whiskers show the locations of either 1.5 × IQR above the third quartile or 1.5 × IQR below the first quartile.

(D) Plot depicting the number of genes with changes in Gini index after C70 treatment.

(E) Top signaling pathways enriched among genes with decreasing Gini index after C70 treatment in MCF7 and FULVR cells.

(F) Shannon's equitability showing a correlation between *KDM5B* gene expression and transcriptomic heterogeneity in ER^+ (n = 808) breast tumors in the TCGA dataset. All tumors are stratified into four groups with identical sample size based on *KDM5B* expression levels from low (1) to high (4).

(G) Shannon's equitability showing a correlation between *KDM5B* gene expression and transcriptomic heterogeneity in ER^+ (n = 108) distant metastases of breast cancer in the Metastatic Breast Cancer Project dataset. Patient stratification is the same as in (F).

(H) Patient survival between high and low transcriptome heterogeneity in all (n = 1,093), ER^+ (n = 808), and ER^- (n = 237) breast tumors in the TCGA data. All patients are stratified into two groups with identical sample size based on the transcriptome heterogeneity.

In (F) and (G), the outer violin indicates the entire distribution, the inner violin in white indicates the IQR, the "." and "+" inside the violin show the median and mean value, respectively. See also Figure S3.

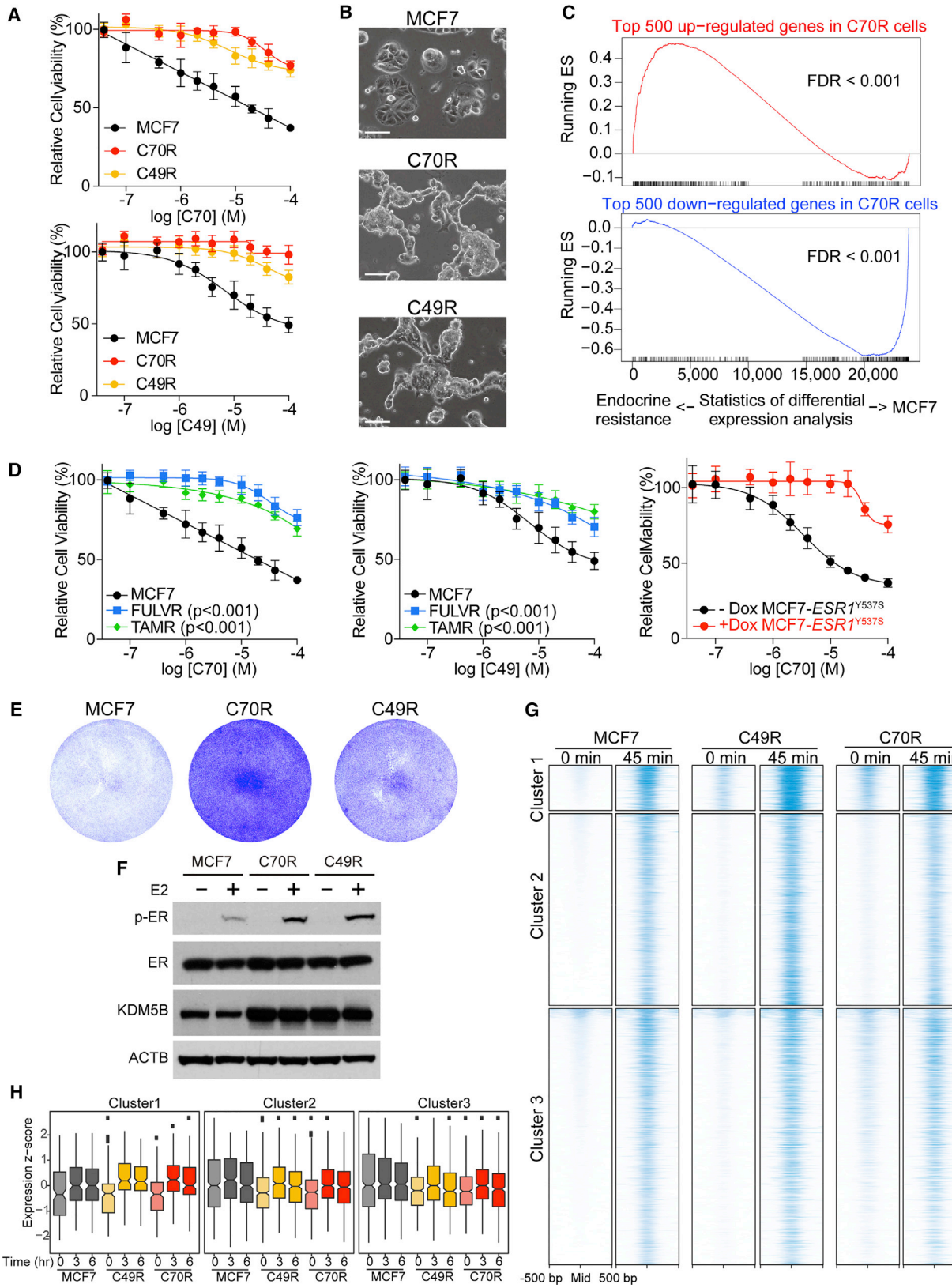

(legend on next page)

We then sought to further explore the potential relatedness of endocrine and KDM5i resistance in ER^+ breast cancer cells. Pathway analysis of genes upregulated in KDM5IR cells compared with KDM5i-treated parental MCF7 cells showed enrichment in ER and androgen receptor signaling (Figure S4D), implying a gain of hormonal responsiveness. Similarly, we confirmed that ER protein levels decreased after short-term C70 treatment in most cell lines, but was close to parental MCF7 levels in C70R and C49R cells (Figures S4E and S4F). In line with this finding, we found that KDM5IR cells can proliferate without estrogen (Figure 4E) and showed higher levels of phosphorylated ER after estradiol (E2) treatment compared with MCF7 cells (Figure 4F). To assess whether these observations are due to alterations in ER chromatin binding in KDM5IR cells, we performed ER ChIP-seq before and after E2 stimulation. MCF7 cells cultured in estrogen-depleted conditions had very few ER binding peaks with a dramatic increase 45 min after E2 stimulation (Figure 4G), which is consistent with previous studies (Figure S4G), although, as expected, some variability was observed among different batches of MCF7 cells (Ben-David et al., 2018). In contrast, in KDM5IR cells a subset of ER binding peaks (cluster 1) was present even in estrogen-depleted conditions and increased to a much higher level after E2 treatment than what was observed in parental cells (Figure 4G). The increased ER binding was functionally relevant as we detected more pronounced upregulation of associated genes following E2 treatment in KDM5IR compared with parental MCF7 cells, especially for cluster 1 genes (Figure 4H; Table S4). Cluster 1 genes also showed significant enrichment for genes highly expressed in KDM5IR cells (Figure S4H) implying that the increased ER binding may contribute to the upregulation of the associated genes. Pathway analysis showed that cluster 1 genes were enriched for glucocorticoid receptor signaling and metabolic processes (Figure S4I), and, thus, their higher basal level and enhanced upregulation following E2 treatment in KDM5i-resistant cells may explain the E2 independence and faster growth of these cells.

To explore other potential changes in the epigenetic landscape of KDM5IR cells in further detail, we performed mass spectrometry analysis of histone modifications. We detected an increase in multiple histone modifications (Figure S4J), which was also confirmed by immunoblotting (Figure S4K). Among all modifications analyzed, only H3K27me3- and H3K27me2-containing peptides were more abundant in both C70R and C49R compared with parental MCF7 cells. Investigating the expression of enzymes that regulate H3K27 methylation in our RNA-seq data revealed a significant (1.5× fold change, $q = 1.5 \times 10^{-6}$) increase of SUZ12, a component of the PRC2 complex that also contains the EZH2 H3K27 methyltransferase (Schuettengruber et al., 2017), which we verified by immunoblot analysis (Figure S4K). To evaluate the role of H3K27me3 upregulation in KDM5i resistance, we then tested the effect of the EZH2 inhibitor GSK126 (McCabe et al., 2012) on sensitivity to KDM5i. We found that treatment with GSK126 decreased global H3K27me3 levels and rendered both C70R and C49R cells more sensitive to KDM5i (Figures S4L and S4M). These results suggest that the increased PRC2 activity and H3K27me3 in KDM5IR cells led to the acquisition of a less-differentiated more basal/stem cell-like epigenetic state (Laugesen and Helin, 2014) associated with decreased sensitivity to KDM5 inhibition. These results also imply that KDM5i resistance is likely due to epigenetic mechanisms.

Single-Cell Profiling of Drug-Resistant Cells

We then explored our scRNA-seq data to determine whether we could detect rare cells with gene expression signatures of drug-resistant cells prior to treatment and whether drug-resistant and drug-treated cells show similar gene expression profiles. Thus, we selected genes differentially expressed between parental MCF7 and FULVR or fulvestrant-treated cells based on bulk RNA-seq data (Figure S5A, Table S5) and investigated if single cells could be classified into one of these three transcriptionally distinct groups (i.e., parental MCF7, FULVR, and MCF7+FULV). While almost all single cells in FULVR population were classified as FULVR, very few such cells were present in parental MCF7 and in fulvestrant-treated cell populations (Figure 5A), implying that drug-resistant clones were selected from a mixed population during treatment. The majority of FULV-treated cells were classified as "MCF7+FULV" and FULVR cells lacked such a cell population, further suggesting that FULVR cells represent a distinct subpopulation (Figure 5A). Similarly, we defined the transcriptional signatures of C70-treated and C70R cells (Figure S5B) and classified single cells into one of the three states (i.e., parental MCF7, C70R, and MCF7+C70). In contrast to FULVR cells, cells classified as "MCF7+C70" were present in the C70R cell population, although the majority of C70R cells had a C70R signature (Figure 5B). In parental MCF7 cells the

Figure 4. Characterization of Acquired KDM5i Resistance

(A) Cellular viability of MCF7, C70R, and C49R cells after treatment with C70 or C49.

(B) Morphology of MCF7, C70R, and C49R cells. Scale bars, 100 μm.

(C) Gene set enrichment analysis (GSEA) plots depicting the relationship between genes in C70R cells and genes in endocrine-resistant cells. Genes are ranked by the statistical significance of differential expression analysis between MCF7 and endocrine-resistant cells (FULVR and TAMR) on the x axis, with up genes in endocrine-resistant cells on the left side. The enrichment score of top 500 up or down genes in C70R compared with MCF7 cells are plotted as red and blue curves, respectively.

(D) Cellular viability after treatment with C70 or C49 in FULVR, TAMR, and MCF7-*ESR1*^{Y537S} cells.

(E) Colony growth of MCF7- and KDM5i-resistant cells in charcoal-stripped medium.

(F) Immunoblot for the indicated proteins following E2 treatment.

(G) ER chromatin binding peaks (±500 bp peak summit) in MCF7, C49R, and C70R cells after estrogen deprivation (0 min) and 45 min after E2 treatment. Only the ER binding peaks responding to E2 treatment in MCF7 cells are shown.

(H) Integrated analysis of associations between gene expression changes at different time points (0–6 hr) after E2 treatment and ER chromatin binding in the indicated clusters and cell lines. The box indicates the IQR, the line inside the box shows the median, and whiskers show the locations of either 1.5 × IQR above the third quartile or 1.5 × IQR below the first quartile.

In (A) and (D), Error bars represent SD, n = 6. See also Figure S4 and Tables S2, S3, and S4.

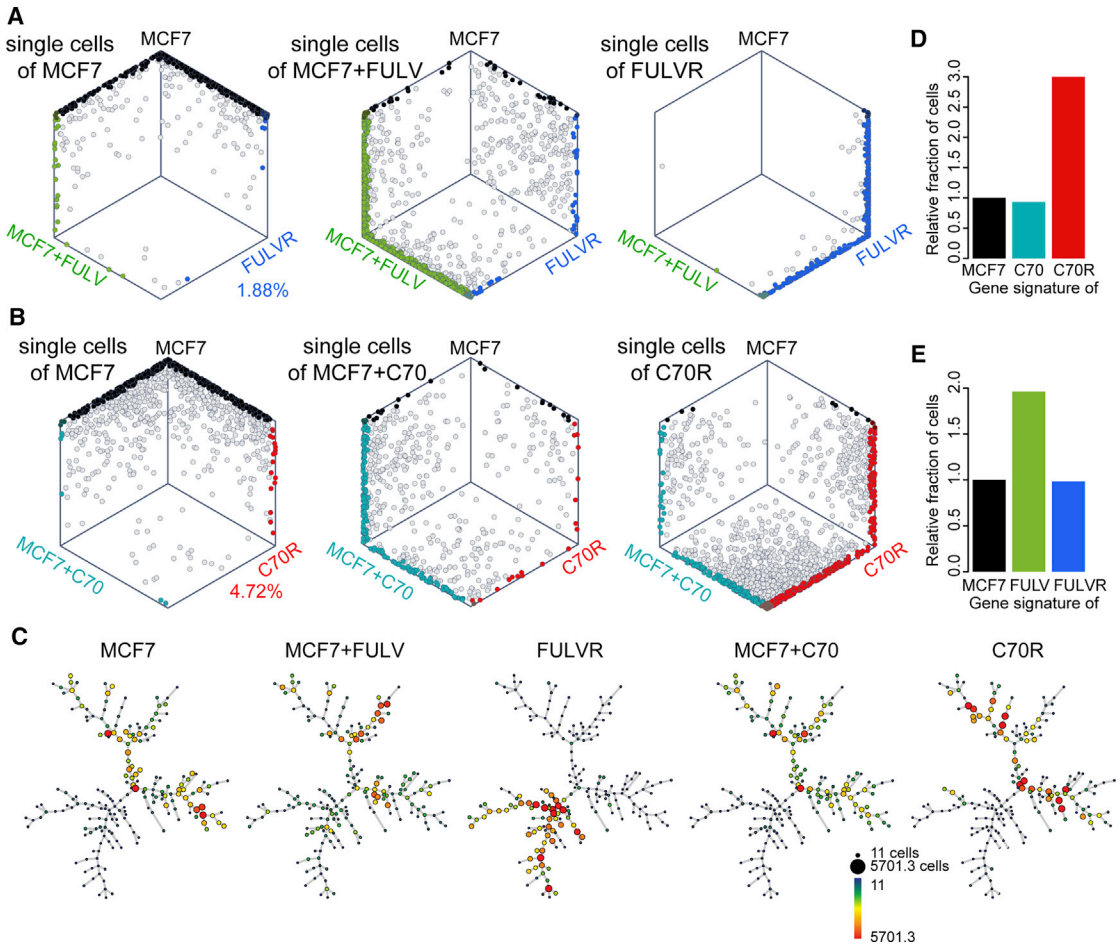

Figure 5. Single-Cell Profiling of Drug-Resistant Cells

(A) Hexagonal plots depicting the bootstrap classification of single cells in populations of MCF7, fulvestrant-treated (MCF7+FULV), and FULVR cells. Each point is one single cell and is positioned along axes according to its bootstrapping classification score for the indicated cell identity. Black, green, and blue cells are classified as MCF7, MCF7+FULV, and FULVR cells, and gray cells are unclassified. A few cells are classified as combination of two cell identities and are represented by mixed color of the two, and positioned at the edges of 2, 6, and 10 o'clock.

(B) Hexagonal plots depicting the bootstrap classification of single cells in populations of MCF7, C70-treated MCF7 (MCF7+C70), and C70R cells. Each point is one single cell and is positioned along axes according to its bootstrapping classification score for the indicated cell identity. Black, light blue, and red cells are classified as MCF7, MCF7+C70, and C70R cells, and gray cells are unclassified. A few cells are classified as combination of two cell identities and are represented by mixed color of the two, and positioned at the edges of 2, 6, and 10 o'clock.

(C) Projection of SPADE tree for each cell line. Colors and size of the node correspond to the percentage of cells that belongs to a given cluster. Light gray dots mark cells with low marker expression in all channels.

(D) Relative proportions of cells in FULVR population with MCF7, MCF7+C70, and C70R gene signature.

(E) Relative proportions of cells in C70R population with MCF7, MCF7+FULV, and FULVR gene signature.

See also Figure S5 and Table S5.

majority of single cells were classified as "parental" with a few cells representing C70R and MCF7+C70 states, while the parental state was rarely detected in C70R cells (Figure 5B). CyTOF experiments also confirmed that FULVR cells represent a very distinct cell population, while fulvestrant- and C70-treated, and C70R cells are more related to parental MCF7 cells (Figure 5C). Thus, two different types of single-cell analysis methods suggested that resistance to fulvestrant is due to selection for a distinct cell population, while resistance to C70 inhibitor treatment is not due to selection for such a cell population but rather attributable to changes in the epigenetic state such as upregulation of H3K27me3 (Figures S4L and S4M).

Lastly, we explored our inDrop data for potential overlaps between endocrine- and KDM5i-resistant cell populations. In line with our observation that FULVR cells are also resistant to KDM5i, we detected an increase in the percent of cells with C70R signature in the FULVR population (Figure 5D). In contrast, the FULVR signature was present in the same fraction of C70R cells as in parental MCF7 population (Figure 5E). Analysis of the cellular expression pattern of selected estrogen-regulated genes (e.g., *TFF1* and *CDKN1A*) and genes related to endocrine (e.g., *SPDEF*) and KDM5i (e.g., *ZMYND8* and *PARP16*) resistance were consistent with these findings (Figure S5C). These molecular data provide a mechanistic explanation for our

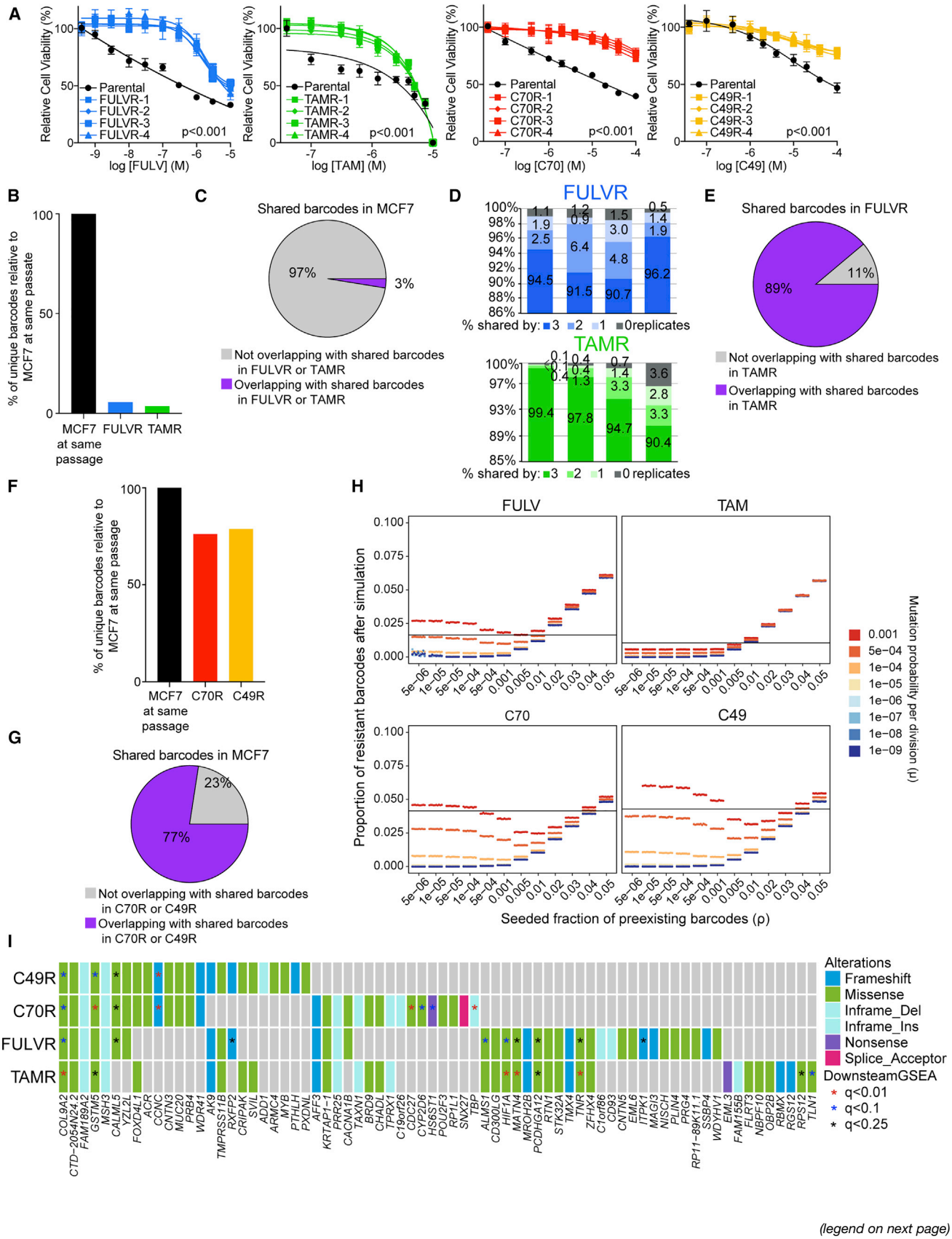

(legend on next page)

functional data on the relatedness of responses and resistance to anti-estrogens and KDM5i.

Modes of Resistance to Anti-estrogens and KDM5i

To investigate whether there is a pre-existing resistant population selected during treatment or a *de novo* acquisition of this phenotype, we labeled MCF7 cells with the ClonTracer barcode library (Bhang et al., 2015), which enables the high-resolution tracking of more than one million cancer cells during drug treatment (Figure S6A). To distinguish pre-existing clones from acquired alterations, four replicates of barcoded cells with comparable starting barcode representations were subjected to long-term inhibitor treatment until resistance was achieved as confirmed by a significant ($p < 0.001$) shift in the IC_{50} curves (Figure 6A). FULVR cells became ER independent as downregulation of ER did not affect their viability (Figures S6B and S6C). If resistance is driven by newly acquired alterations, distinct barcoded populations would emerge in independent replicates, while if pre-existing clones were the major source of resistance, there should be selective enrichment for the same sets of barcodes in multiple replicates. The treatment with FULV or TAM significantly reduced the barcode complexity (Figures 6B,6C, and S6D) and more than 90% of the barcodes were shared by all four replicates (Figures 6D and S6E). These findings strongly indicate that the vast majority of fulvestrant- and TAMR-resistant clones were pre-existing in the parental MCF7 cell population and were highly selected during treatment. Moreover, the barcodes found in FULVR clones appeared to be largely overlapping with the barcodes found in TAMR clones (Figure 6E), indicating that these two different endocrine therapies select for the same pre-existing cell population. In contrast, there was minimal selection during C70 and C49 treatment since the barcode pool of the KDM5i-resistant population was not appreciably different from parental MCF7 cells at the same passage (Figures 6F,6G, S6D, and S6E), suggesting that resistance to KDM5i is not due to selection for pre-existing resistant cells.

We then performed mathematical modeling of the barcode data in order to estimate the fraction of pre-existing barcodes in the FULVR, TAMR, C70R, and C49R cells. We utilized a stochastic population dynamics model (Bhang et al., 2015; McDonald and Michor, 2017) parameterized using the growth kinetics of parental as well as endocrine and KDM5IR cells (Figure 6H). For each experimental condition, we performed ten independent runs of the stochastic simulations (see the STAR Methods) and estimated the fraction of pre-existing barcodes for each condition and for different estimates of the rates per cell division that generate a resistant cell type from the parental population. Given the experimentally observed high fraction of resistant barcodes shared by replicates relative to parental cells (FULV:MCF7 ratio = 23.94) (Figure S6F), we found that expected rates of generating resistant cell types (mutation probability) were less than 10^{-5} per cell division in FULV treatment (Figure S6G), which is in agreement with experimental findings showing the selection of pre-existing resistant clones. At this mutation probability, we identified the fraction of pre-existing barcodes between 0.5% and 1.0% for FULVR (Figure S6G) based on the horizontal line showing the proportion of pre-existing resistant barcodes identified in the experiment (Figure 6H). Similarly, we identified the pre-existing proportion of barcodes as around 1.0% for TAMR populations at a similar mutation probability. In C70R and C49R cells, we found that the larger mutation rate (0.05%–0.1% mutations per cell division) fits to the horizontal line (Figure 6H) to recapitulate the observed proportion of about 4%. Finally, to determine if the resistant cell populations were genetically distinct, we performed exome sequencing of resistant and parental MCF7 cells and also sequenced the lentiviral integration sites. We found numerous genetic variants present in both fulvestrant- and TAMR-resistant cells, and gene set enrichment analysis showed that the expression of genes downstream of some of the genetic variants were significantly altered (Figure 6I; Table S6). Several of the genetic variants found in both FULVR and TAMR cells were related to glutamate metabolism (e.g., *HIF1A*, *PCDHGA12*, *TMX4*, and *TNR*) and almost all of them were also detected in metastatic lesions of breast cancer patients resistant to endocrine therapies (Cohen et al., 2017) confirming their physiologic relevance.

DISCUSSION

Hormone-dependent ER^+ luminal tumors constitute the most common subtype representing ~70% of all breast cancer cases. Although endocrine therapies are effective for the treatment of both early and advanced-stage disease, inherent and acquired resistance is a major clinical challenge (Osborne and Schiff, 2011). Numerous mechanisms have been proposed to explain endocrine resistance including changes in ER regulators and growth factor signaling pathways (Musgrove and Sutherland, 2009; Osborne and Schiff, 2011). Exome sequencing of

Figure 6. Resistance to Anti-estrogens and KDM5i in MCF7 Cells

(A) Cellular viability after treatment with C70 and C49, fulvestrant, or tamoxifen in parental and cells with acquired resistance to the indicated agents. Error bars represent SD, n = 6.

(B) Bar graph depicting percentage of unique barcodes in FULVR and TAMR relative to parental MCF7 cells at same passage.

(C) Pie chart depicting percentage of barcodes overlapping between MCF7 and FULVR/TAMR cells.

(D) Bar graph depicting percentage of total barcodes shared among all replicates in each of the indicated cell populations.

(E) Pie chart depicting percentage of barcodes overlapping between FULVR and TAMR.

(F) Bar graph depicting percentage of unique barcodes in C70R and C49R relative to MCF7 cells at same passage.

(G) Pie chart depicting percentage of barcodes overlapping between MCF7 and C70R/C49R cells.

(H) Panels show model-predicted percentages of total barcodes shared by quadruplicates after simulation for different mutation probabilities (μ) and seeded fractions of pre-existing resistant barcodes (ρ) in the treatment with the indicated inhibitors compared with the same statistic from the experimental data (horizontal line). The growth rates in simulations were based on experimental data.

(I) Mutated genes detected in resistant but not in MCF7 cells. Colors and stars indicate the type of mutations and significance of downstream GSEA in the corresponding resistant cell lines, respectively. The significance of downstream GSEA represents the downstream genes of mutations are significantly enriched in up-/downregulated genes in the corresponding resistant cell lines. See also Figure S6 and Table S6.

metastatic lesions in endocrine-resistant disease identified *ESR1* mutations, implying that genetic alterations are likely to be responsible for resistance in a subset of cases (Jeselsohn et al., 2017). We have previously shown that a high KDM5B PARADIGM (Vaske et al., 2010) activity score is associated with shorter disease-specific survival in endocrine therapy-treated ER$^+$ breast cancer patients, implicating KDM5B in endocrine resistance (Yamamoto et al., 2014). Here we describe a comprehensive characterization of mechanisms of response and resistance to KDM5 inhibitors and their relevance for endocrine sensitivity. We found that inhibition of *KDM5B* and *KDM5A* increases sensitivity to fulvestrant in both hormone-sensitive and endocrine-resistant cells. Single-cell analysis of drug-sensitive and resistant populations using inDrop and CyTOF as well as lentiviral barcoding confirmed that endocrine resistance is due to the selection for a pre-existing distinct cell population.

Despite the importance of intratumor phenotypic heterogeneity for tumor progression and therapy resistance (Marusyk et al., 2012; Marusyk and Polyak, 2010), our understanding of regulators of this process and our ability to modulate them are very limited. Recent advances in genomic sequencing and single-cell technologies have enabled the detailed characterization of tumors at the single-cell level (Macaulay et al., 2017). Although most of the single-cell studies thus far have focused on defining individual cell types (Tirosh et al., 2016), scRNA-seq has also been used to characterize cell-to-cell variability in immune cells in aging (Martinez-Jimenez et al., 2017). Epigenetic regulators such as histone modifying enzymes are critical for the establishment of cell-type-specific gene expression patterns, and, thus, they are also likely to play a role in modulating cell-to-cell variability in transcription, but this has been mostly investigated in lower-level organisms during aging (Booth and Brunet, 2016). We have previously shown that neoplastic and stem cell-like mammary epithelial cells have higher transcriptomic diversity than normal and more differentiated cells based on the analysis of bulk gene expression data (Wu et al., 2010). Here we describe that KDM5 histone demethylase is a regulator of cellular transcriptomic heterogeneity in ER$^+$ luminal breast cancer, and its higher expression in ER$^+$ breast tumors is associated with higher transcriptomic, but not genetic, heterogeneity and shorter overall survival. Higher cell-to-cell variability increases the probability of therapeutic resistance (Chisholm et al., 2016). Most studies analyzing intratumor heterogeneity have focused on genetic alterations and in many cases therapeutic resistance is due to mutations in genes and pathways targeted by the treatment (McGranahan and Swanton, 2017). However, non-genetic variability such as epigenetic heterogeneity also contributes to therapeutic resistance by multiple different mechanisms (Brock et al., 2009). One possibility is that the distinct epigenetic state of the cells could determine cellular response to treatment (Shibue and Weinberg, 2017). Another option is that subpopulations of phenotypically different cells (e.g., persisters) provide a temporary pool for selection during treatment and facilitate the outgrowth of drug-resistant mutants as demonstrated by the emergence of EGFR(T790M)-positive clones from drug-tolerant subpopulations of lung cancer cells (Hata et al., 2016). Because KDM5 activity regulates both differentiated luminal epithelial epigenetic states and cellular transcriptomic diversity, KDM5i could decrease the probability of therapeutic resistance in different ways in multiple different cancer types including ER$^+$ luminal breast cancers.

In summary, our data highlight the importance of cellular phenotypic heterogeneity in therapeutic responses and identifies members of the KDM5 HDM family as key epigenetic regulators of this process suggesting that inhibiting KDM5 activity could decrease resistance to cancer therapies.

STAR★METHODS

Detailed methods are provided in the online version of this paper and include the following:

- KEY RESOURCES TABLE
- CONTACT FOR REAGENT AND RESOURCE SHARING
- EXPERIMENTAL MODEL AND SUBJECT DETAILS
  - Breast Cancer Cohort Data
  - Breast Cancer Cell Lines
  - Barcoding and Selection for Resistant Cells
  - Animal Model
- METHOD DETAILS
  - Cellular Viability Assay
  - ChIP-seq and RNA-seq
  - Xenograft Assays
  - Immunoblotting
  - Immunofluorescence Analyses
  - Antibodies and Inhibitors
  - CRISPR Experiments
  - inDrop
  - Mass Cytometry
  - Mass Spectrometry Analysis of Histone Modifications
- QUANTIFICATION AND STATISTICAL ANALYSIS
  - ChIP-seq Analysis
  - RNA-seq Analysis
  - Barcoding Data Analysis
  - Exome Sequencing
  - Resistant Cell-specific Mutations and Downstream GSEA Analysis
  - Genetic Heterogeneity and Clonality Analysis of Cell Lines
  - Transcriptomic Heterogeneity Estimation in Clinical Samples
  - Width versus Height Analysis of Histone Marks
  - inDrop Data Analysis
  - Gene Set Enrichment Analysis (GSEA)
  - Simulation Methods
  - Estimation of Parameters for Simulation
- DATA AND SOFTWARE AVAILABILITY

SUPPLEMENTAL INFORMATION

Supplemental Information includes six figures and six tables can be found with this article online at https://doi.org/10.1016/j.ccell.2018.10.014.

ACKNOWLEDGMENTS

We thank members of our laboratories for their critical reading of this manuscript and useful discussions. We thank members of Allon Klein's laboratory and the Single Cell Core at Harvard Medical School, particularly Allon Klein,

Rapolas Zilionis, Sarah Boswell, and Alex Ratner, for providing instructions and guidance for setting up our single-cell RNA sequencing system. We thank Bob Yauch (Genentech, San Francisco) for providing us the KDM5 inhibitor 48 and the Lurie Family Imaging Center for performing the *in vivo* xenograft experiments. This research was supported by the National Cancer Institute PSOC U54 CA193461 (to F.M. and K.P.), R35 CA197623 (to K.P.), P01 CA080111 (to K.P., M.B., and P.S.), R01 CA202634 (to P.S.), the Ludwig Center at Harvard (to K.P., F.M., and M.B.), and the Division of Preclinical Innovation of the National Center for Advancing Translational Sciences (NCATS), NIH (to S.C.K., A.S., D.J.M., G.R., A.J., and M.L.-N.).

AUTHOR CONTRIBUTIONS

K.H., S.V., K.J.I., T.M., A.F., S.B.E., M.P., L.D., and G.P. performed ChIP-seq, RNA-seq, cell culture, and CyTOF experiments. K.H., H.-J.W., S.V., T.O.McD., K.N.Y., O.C., and S.B.E. completed data analyses and software development. S.C.K., M.L.-N., G.R., D.J.M., A.J., A.S., R.J., M.B., N.W., A.M., P.S., J.D.J., and A.A.G. provided reagents and resources. K.P. and F.M. supervised the study. All authors helped to design the study and write the manuscript.

DECLARATION OF INTERESTS

P.S., M.B., N.W., and K.P. received research support and were consultants to Novartis Institutes for BioMedical Research during the execution of this study. K.P. and M.B. serves on the scientific advisory board of Mitra Biotech and Kronos Bio, respectively. R.J. receives research support from Pfizer. N.W. was a shareholder of Foundation Medicine and a consultant to Eli Lilly during the execution of this study, and he currently receives research support from Puma Biotechnologies. L.D. is current employee of Cugene.

Received: December 22, 2017
Revised: August 17, 2018
Accepted: October 25, 2018
Published: November 21, 2018; corrected online: February 1, 2019

REFERENCES

Anders, S., Pyl, P.T., and Huber, W. (2015). HTSeq – a Python framework to work with high-throughput sequencing data. Bioinformatics *31*, 166–169.

Ben-David, U., Siranosian, B., Ha, G., Tang, H., Oren, Y., Hinohara, K., Strathdee, C.A., Dempster, J., Lyons, N.J., Burns, R., et al. (2018). Genetic and transcriptional evolution alters cancer cell line drug response. Nature *560*, 325–330.

Benayoun, B.A., Pollina, E.A., Ucar, D., Mahmoudi, S., Karra, K., Wong, E.D., Devarajan, K., Daugherty, A.C., Kundaje, A.B., Mancini, E., et al. (2014). H3K4me3 breadth is linked to cell identity and transcriptional consistency. Cell *158*, 673–688.

Bendall, S.C., Simonds, E.F., Qiu, P., Amir el, A.D., Krutzik, P.O., Finck, R., Bruggner, R.V., Melamed, R., Trejo, A., Ornatsky, O.I., et al. (2011). Single-cell mass cytometry of differential immune and drug responses across a human hematopoietic continuum. Science *332*, 687–696.

Bhang, H.E., Ruddy, D.A., Krishnamurthy Radhakrishna, V., Caushi, J.X., Zhao, R., Hims, M.M., Singh, A.P., Kao, I., Rakiec, D., Shaw, P., et al. (2015). Studying clonal dynamics in response to cancer therapy using high-complexity barcoding. Nat. Med. *21*, 440–448.

Booth, L.N., and Brunet, A. (2016). The aging epigenome. Mol. Cell *62*, 728–744.

Brastianos, P.K., Horowitz, P.M., Santagata, S., Jones, R.T., McKenna, A., Getz, G., Ligon, K.L., Palescandolo, E., Van Hummelen, P., Ducar, M.D., et al. (2013). Genomic sequencing of meningiomas identifies oncogenic SMO and AKT1 mutations. Nat. Genet. *45*, 285–289.

Brock, A., Chang, H., and Huang, S. (2009). Non-genetic heterogeneity – a mutation-independent driving force for the somatic evolution of tumours. Nat. Rev. Genet. *10*, 336–342.

Chanrion, M., Negre, V., Fontaine, H., Salvetat, N., Bibeau, F., Mac Grogan, G., Mauriac, L., Katsaros, D., Molina, F., Theillet, C., and Darbon, J.M. (2008). A gene expression signature that can predict the recurrence of tamoxifen-treated primary breast cancer. Clin. Cancer Res. *14*, 1744–1752.

Chisholm, R.H., Lorenzi, T., and Clairambault, J. (2016). Cell population heterogeneity and evolution towards drug resistance in cancer: biological and mathematical assessment, theoretical treatment optimisation. Biochim. Biophys. Acta *1860*, 2627–2645.

Cibulskis, K., Lawrence, M.S., Carter, S.L., Sivachenko, A., Jaffe, D., Sougnez, C., Gabriel, S., Meyerson, M., Lander, E.S., and Getz, G. (2013). Sensitive detection of somatic point mutations in impure and heterogeneous cancer samples. Nat. Biotechnol. *31*, 213–219.

Cohen, O., Kim, D., Oh, C., Waks, A., Oliver, N., Helvie, K., Marini, L., Rotem, A., Lloyd, M., Stover, D., et al. (2017). Whole exome and transcriptome sequencing of resistant ER+ metastatic breast cancer. Cancer Res. *77* (4 Suppl), Abstract no. S1–01.

Creech, A.L., Taylor, J.E., Maier, V.K., Wu, X., Feeney, C.M., Udeshi, N.D., Peach, S.E., Boehm, J.S., Lee, J.T., Carr, S.A., and Jaffe, J.D. (2015). Building the connectivity map of epigenetics: chromatin profiling by quantitative targeted mass spectrometry. Methods *72*, 57–64.

DePristo, M.A., Banks, E., Poplin, R., Garimella, K.V., Maguire, J.R., Hartl, C., Philippakis, A.A., del Angel, G., Rivas, M.A., Hanna, M., et al. (2011). A framework for variation discovery and genotyping using next-generation DNA sequencing data. Nat. Genet. *43*, 491–498.

Feinberg, A.P., Koldobskiy, M.A., and Gondor, A. (2016). Epigenetic modulators, modifiers and mediators in cancer aetiology and progression. Nat. Rev. Genet. *17*, 284–299.

Flavahan, W.A., Gaskell, E., and Bernstein, B.E. (2017). Epigenetic plasticity and the hallmarks of cancer. Science *357*, https://doi.org/10.1126/science.aal2380.

Gerlinger, M., McGranahan, N., Dewhurst, S.M., Burrell, R.A., Tomlinson, I., and Swanton, C. (2014). Cancer: evolution within a lifetime. Annu. Rev. Genet. *48*, 215–236.

Hata, A.N., Niederst, M.J., Archibald, H.L., Gomez-Caraballo, M., Siddiqui, F.M., Mulvey, H.E., Maruvka, Y.E., Ji, F., Bhang, H.E., Krishnamurthy Radhakrishna, V., et al. (2016). Tumor cells can follow distinct evolutionary paths to become resistant to epidermal growth factor receptor inhibition. Nat. Med. *22*, 262–269.

Horton, J.R., Engstrom, A., Zoeller, E.L., Liu, X., Shanks, J.R., Zhang, X., Johns, M.A., Vertino, P.M., Fu, H., and Cheng, X. (2016). Characterization of a linked Jumonji domain of the KDM5/JARID1 family of histone H3 lysine 4 demethylases. J. Biol. Chem. *291*, 2631–2646.

Huang, S. (2013). Genetic and non-genetic instability in tumor progression: link between the fitness landscape and the epigenetic landscape of cancer cells. Cancer Metastasis Rev. *32*, 423–448.

Jeselsohn, R., Buchwalter, G., De Angelis, C., Brown, M., and Schiff, R. (2015). ESR1 mutations—a mechanism for acquired endocrine resistance in breast cancer. Nat. Rev. Clin. Oncol. *12*, 573–583.

Jeselsohn, R., De Angelis, C., Brown, M., and Schiff, R. (2017). The evolving role of the estrogen receptor mutations in endocrine therapy-resistant breast cancer. Curr. Oncol. Rep. *19*, 35.

Jiang, L., Chen, H., Pinello, L., and Yuan, G.C. (2016). GiniClust: detecting rare cell types from single-cell gene expression data with Gini index. Genome Biol. *17*, 144.

Johansson, C., Velupillai, S., Tumber, A., Szykowska, A., Hookway, E.S., Nowak, R.P., Strain-Damerell, C., Gileadi, C., Philpott, M., Burgess-Brown, N., et al. (2016). Structural analysis of human KDM5B guides histone demethylase inhibitor development. Nat. Chem. Biol. *12*, 539–545.

Kim, D., Pertea, G., Trapnell, C., Pimentel, H., Kelley, R., and Salzberg, S.L. (2013). TopHat2: accurate alignment of transcriptomes in the presence of insertions, deletions and gene fusions. Genome Biol. *14*, R36.

Landau, D.A., Carter, S.L., Stojanov, P., McKenna, A., Stevenson, K., Lawrence, M.S., Sougnez, C., Stewart, C., Sivachenko, A., Wang, L., et al. (2013). Evolution and impact of subclonal mutations in chronic lymphocytic leukemia. Cell *152*, 714–726.

Laugesen, A., and Helin, K. (2014). Chromatin repressive complexes in stem cells, development, and cancer. Cell Stem Cell *14*, 735–751.

Li, H., and Durbin, R. (2009). Fast and accurate short read alignment with Burrows-Wheeler transform. Bioinformatics *25*, 1754–1760.

Li, H., Handsaker, B., Wysoker, A., Fennell, T., Ruan, J., Homer, N., Marth, G., Abecasis, G., and Durbin, R.; 1000 Genome Project Data Processing Subgroup (2009). The sequence alignment/map format and SAMtools. Bioinformatics *25*, 2078–2079.

Li, N., Li, Y., Lv, J., Zheng, X., Wen, H., Shen, H., Zhu, G., Chen, T.Y., Dhar, S.S., Kan, P.Y., et al. (2016). ZMYND8 reads the dual histone mark H3K4me1-H3K14ac to antagonize the expression of metastasis-linked genes. Mol. Cell *63*, 470–484.

Liang, J., Zhang, B., Labadie, S., Ortwine, D.F., Vinogradova, M., Kiefer, J.R., Gehling, V.S., Harmange, J.C., Cummings, R., Lai, T., et al. (2016). Lead optimization of a pyrazolo[1,5-a]pyrimidin-7(4H)-one scaffold to identify potent, selective and orally bioavailable KDM5 inhibitors suitable for in vivo biological studies. Bioorg. Med. Chem. Lett. *26*, 4036–4041.

Lohr, J.G., Stojanov, P., Carter, S.L., Cruz-Gordillo, P., Lawrence, M.S., Auclair, D., Sougnez, C., Knoechel, B., Gould, J., Saksena, G., et al. (2014). Widespread genetic heterogeneity in multiple myeloma: implications for targeted therapy. Cancer Cell *25*, 91–101.

Love, M.I., Huber, W., and Anders, S. (2014). Moderated estimation of fold change and dispersion for RNA-seq data with DESeq2. Genome Biol. *15*, 550.

Lun, A.T., Bach, K., and Marioni, J.C. (2016). Pooling across cells to normalize single-cell RNA sequencing data with many zero counts. Genome Biol. *17*, 75.

Macaulay, I.C., Ponting, C.P., and Voet, T. (2017). Single-cell multiomics: multiple measurements from single cells. Trends Genet. *33*, 155–168.

Martinez-Jimenez, C.P., Eling, N., Chen, H.C., Vallejos, C.A., Kolodziejczyk, A.A., Connor, F., Stojic, L., Rayner, T.F., Stubbington, M.J.T., Teichmann, S.A., et al. (2017). Aging increases cell-to-cell transcriptional variability upon immune stimulation. Science *355*, 1433–1436.

Marusyk, A., Almendro, V., and Polyak, K. (2012). Intra-tumour heterogeneity: a looking glass for cancer? Nat. Rev. Cancer *12*, 323–334.

Marusyk, A., and Polyak, K. (2010). Tumor heterogeneity: causes and consequences. Biochim. Biophys. Acta *1805*, 105–117.

McCabe, M.T., Ott, H.M., Ganji, G., Korenchuk, S., Thompson, C., Van Aller, G.S., Liu, Y., Graves, A.P., Della Pietra, A., 3rd, Diaz, E., et al. (2012). EZH2 inhibition as a therapeutic strategy for lymphoma with EZH2-activating mutations. Nature *492*, 108–112.

McDonald, T.O., and Michor, F. (2017). SIApopr: a computational method to simulate evolutionary branching trees for analysis of tumor clonal evolution. Bioinformatics *33*, 2221–2223.

McGranahan, N., Favero, F., de Bruin, E.C., Birkbak, N.J., Szallasi, Z., and Swanton, C. (2015). Clonal status of actionable driver events and the timing of mutational processes in cancer evolution. Sci. Transl. Med. *7*, 283ra254.

McGranahan, N., and Swanton, C. (2017). Clonal heterogeneity and tumor evolution: past, present, and the future. Cell *168*, 613–628.

McKenna, A., Hanna, M., Banks, E., Sivachenko, A., Cibulskis, K., Kernytsky, A., Garimella, K., Altshuler, D., Gabriel, S., Daly, M., and DePristo, M.A. (2010). The genome analysis toolkit: a MapReduce framework for analyzing next-generation DNA sequencing data. Genome Res. *20*, 1297–1303.

McLaren, W., Pritchard, B., Rios, D., Chen, Y., Flicek, P., and Cunningham, F. (2010). Deriving the consequences of genomic variants with the Ensembl API and SNP effect predictor. Bioinformatics *26*, 2069–2070.

Musgrove, E.A., and Sutherland, R.L. (2009). Biological determinants of endocrine resistance in breast cancer. Nat. Rev. Cancer *9*, 631–643.

Olshen, A.B., Venkatraman, E.S., Lucito, R., and Wigler, M. (2004). Circular binary segmentation for the analysis of array-based DNA copy number data. Biostatistics *5*, 557–572.

Osborne, C.K., and Schiff, R. (2011). Mechanisms of endocrine resistance in breast cancer. Annu. Rev. Med. *62*, 233–247.

Roesch, A., Fukunaga-Kalabis, M., Schmidt, E.C., Zabierowski, S.E., Brafford, P.A., Vultur, A., Basu, D., Gimotty, P., Vogt, T., and Herlyn, M. (2010). A temporarily distinct subpopulation of slow-cycling melanoma cells is required for continuous tumor growth. Cell *141*, 583–594.

Roesch, A., Vultur, A., Bogeski, I., Wang, H., Zimmermann, K.M., Speicher, D., Korbel, C., Laschke, M.W., Gimotty, P.A., Philipp, S.E., et al. (2013). Overcoming intrinsic multidrug resistance in melanoma by blocking the mitochondrial respiratory chain of slow-cycling JARID1B(high) cells. Cancer Cell *23*, 811–825.

Schuettengruber, B., Bourbon, H.M., Di Croce, L., and Cavalli, G. (2017). Genome regulation by polycomb and trithorax: 70 years and counting. Cell *171*, 34–57.

Sharma, S.V., Lee, D.Y., Li, B., Quinlan, M.P., Takahashi, F., Maheswaran, S., McDermott, U., Azizian, N., Zou, L., Fischbach, M.A., et al. (2010). A chromatin-mediated reversible drug-tolerant state in cancer cell subpopulations. Cell *141*, 69–80.

Shen, R., and Seshan, V.E. (2016). FACETS: allele-specific copy number and clonal heterogeneity analysis tool for high-throughput DNA sequencing. Nucleic Acids Res. *44*, e131.

Shibue, T., and Weinberg, R.A. (2017). EMT, CSCs, and drug resistance: the mechanistic link and clinical implications. Nat. Rev. Clin. Oncol. *14*, 611–629.

Cancer Genome Atlas Network (2012). Comprehensive molecular portraits of human breast tumours. Nature *490*, 61–70.

Tirosh, I., Izar, B., Prakadan, S.M., Wadsworth, M.H., 2nd, Treacy, D., Trombetta, J.J., Rotem, A., Rodman, C., Lian, C., Murphy, G., et al. (2016). Dissecting the multicellular ecosystem of metastatic melanoma by single-cell RNA-seq. Science *352*, 189–196.

Tumber, A., Nuzzi, A., Hookway, E.S., Hatch, S.B., Velupillai, S., Johansson, C., Kawamura, A., Savitsky, P., Yapp, C., Szykowska, A., et al. (2017). Potent and selective KDM5 inhibitor stops cellular demethylation of H3K4me3 at transcription start sites and proliferation of MM1S myeloma cells. Cell Chem. Biol. *24*, 371–380.

Van der Auwera, G.A., Carneiro, M.O., Hartl, C., Poplin, R., Del Angel, G., Levy-Moonshine, A., Jordan, T., Shakir, K., Roazen, D., Thibault, J., et al. (2013). From FastQ data to high confidence variant calls: the genome analysis toolkit best practices pipeline. Curr Protoc Bioinformatics *43*, 11.10.11–11.10.33.

Vaske, C.J., Benz, S.C., Sanborn, J.Z., Earl, D., Szeto, C., Zhu, J., Haussler, D., and Stuart, J.M. (2010). Inference of patient-specific pathway activities from multi-dimensional cancer genomics data using PARADIGM. Bioinformatics *26*, i237–i245.

Vinogradova, M., Gehling, V.S., Gustafson, A., Arora, S., Tindell, C.A., Wilson, C., Williamson, K.E., Guler, G.D., Gangurde, P., Manieri, W., et al. (2016). An inhibitor of KDM5 demethylases reduces survival of drug-tolerant cancer cells. Nat. Chem. Biol. *12*, 531–538.

Wu, Z.J., Meyer, C.A., Choudhury, S., Shipitsin, M., Maruyama, R., Bessarabova, M., Nikolskaya, T., Sukumar, S., Schwartzman, A., Liu, J.S., et al. (2010). Gene expression profiling of human breast tissue samples using SAGE-Seq. Genome Res. *20*, 1730–1739.

Yamamoto, S., Wu, Z., Russnes, H.G., Takagi, S., Peluffo, G., Vaske, C., Zhao, X., Moen Vollan, H.K., Maruyama, R., Ekram, M.B., et al. (2014). JARID1B is a luminal lineage-driving oncogene in breast cancer. Cancer Cell *25*, 762–777.

Zhang, Y., Liu, T., Meyer, C.A., Eeckhoute, J., Johnson, D.S., Bernstein, B.E., Nusbaum, C., Myers, R.M., Brown, M., Li, W., and Liu, X.S. (2008). Model-based analysis of ChIP-Seq (MACS). Genome Biol. *9*, R137.

Zilionis, R., Nainys, J., Veres, A., Savova, V., Zemmour, D., Klein, A.M., and Mazutis, L. (2017). Single-cell barcoding and sequencing using droplet microfluidics. Nat. Protoc. *12*, 44–73.

STAR★METHODS

KEY RESOURCES TABLE

REAGENT or RESOURCE	SOURCE	IDENTIFIER
Antibodies		
Rabbit polyclonal anti-KDM5B	Sigma-Aldrich	Cat# HPA027179; RRID: AB_1851987
Rabbit polyclonal anti-KDM5B	Novus	Cat# 22260002; RRID: AB_10004656
Mouse monoclonal anti-H3K4me3	Abcam	Cat# ab1012; RRID: AB_442796
Rabbit polyclonal anti-H3K4me2	Millipore	Cat# 07-030; RRID: AB_10099880
Rabbit polyclonal anti-H3K4me1	Abcam	Cat# ab8895; RRID: AB_306847
Rabbit polyclonal anti-Histone H3	Abcam	Cat# ab1791; RRID: AB_302613
Mouse monoclonal anti-beta-Actin	Sigma-Aldrich	Cat# A2228; RRID: AB_476697
Rabbit polyclonal anti-H3K27Ac	Abcam	Cat# ab4729; RRID: AB_2118291
Mouse monoclonal anti-H3K27me3	Abcam	Cat# ab6002; RRID: AB_305237
Rabbit polyclonal anti-H3K27me2	Abcam	Cat# ab24684; RRID: AB_448222
Rabbit polyclonal anti-H3K36me2	Abcam	Cat# ab9049; RRID: AB_1280939
Rabbit polyclonal anti-H3K9Ac	Abcam	Cat# ab4441; RRID: AB_2118292
Rabbit polyclonal anti-H3K79me2	Abcam	Cat# ab3594; RRID: AB_303937
Rabbit monoclonal anti-SUZ12	Cell Signaling Technology	Cat# 3737; RRID: AB_2196850
Rabbit monoclonal anti-ERα	Cell Signaling Technology	Cat# 8644; RRID: AB_2617128
Mouse monoclonal anti-phospho-ERα Ser118	Cell Signaling Technology	Cat# 2511; RRID: AB_331289
Rabbit polyclonal anti-Cleaved Caspase-3 (Asp175)	Cell Signaling Technology	Cat# 9661; RRID: AB_2341188
Rabbit polyclonal anti-Histone H3 (phospho S10)	Abcam	Cat# ab5176; RRID: AB_304763
Rabbit polyclonal anti-H3K4me3	Abcam	Cat# 8580; RRID: AB_306649
Goat anti-rabbit IgG (H+L) conjugated to Alexa Fluor 488	Thermo Fisher Scientific	Cat# A-11034; RRID: AB_2576217
Rabbit monoclonal anti-PR a/b (141Pr)	Cell Signaling Technology	Cat# 8757
Mouse monoclonal anti-CD10 (142Nd)	BD Biosciences	Cat# 555373; RRID: AB_395775
Rat monoclonal anti-CD44 (143Nd)	Biolegend	Cat# 103002; RRID: AB_312953
Mouse monoclonal anti-cyclin D3 (144Nd)	Abcam	Cat# ab28283; RRID: AB_2070798
Mouse monoclonal anti-Muc1 (145Nd)	Biolegend	Cat# 355602; RRID: AB_2561642
Mouse monoclonal anti-Lamp2 (146Nd)	Biolegend	Cat# 354302; RRID: AB_11204245
Mouse monoclonal anti-CDK4 (147Sm)	BD Biosciences	Cat# 559677; RRID: AB_397299
Rabbit monoclonal anti-PTEN (148Nd)	Cell Signaling Technology	Cat# 9559; RRID: AB_390810
Rabbit monoclonal anti-E-Cadherin (149Sm)	Cell Signaling Technology	Cat# 3195; RRID: AB_2291471
Mouse monoclonal anti-Epcam (150Nd)	Biolegend	Cat# 324202; RRID: AB_756076
Mouse monoclonal anti-Her2 (151Eu)	BD Biosciences	Cat# 554299; RRID: AB_395352
Rabbit polyclonal anti-CK5 (152Sm)	Abcam	Cat# ab53121; RRID: AB_869889
Mouse monoclonal anti-CD24 (153Eu)	Biolegend	Cat# 311102; RRID: AB_314851
Mouse monoclonal anti-CDK1 (154Sm)	Biolegend	Cat# 626901; RRID: AB_2074779
Rabbit monoclonal anti-CDK6 (155Gd)	Cell Signaling Technology	Cat# 13331; RRID: AB_2721897
Rabbit monoclonal anti-p63 (158Gd)	Abcam	Cat# ab124762; RRID: AB_10971840
Rabbit monoclonal anti-TCF7 (159Tb)	Cell Signaling Technology	Cat# 2203; RRID: AB_2199302
Rabbit monoclonal anti-AR (160Gd)	Cell Signaling Technology	Cat# 5153; RRID: AB_10691711
Mouse monoclonal anti-Cyclin A (161Dy)	BD Biosciences	Cat# 554175; RRID: AB_395286
Mouse monoclonal anti-Ki-67 (162Dy)	BD Biosciences	Cat# 550609; RRID: AB_393778
Mouse monoclonal anti-SMA (163Dy)	Thermo Fisher Scientific	Cat# 14-9760-82; RRID: AB_2572996
Mouse monoclonal anti-cPARP (164Dy)	BD Biosciences	Cat# 552596; RRID: AB_394437
Rabbit monoclonal anti-Vimentin (165Ho)	Cell Signaling Technology	Cat# 5741; RRID: AB_10695459

(*Continued on next page*)

Continued

REAGENT or RESOURCE	SOURCE	IDENTIFIER
Rat monoclonal anti-GATA-3 (166Er)	eBioscience	Cat# 14-9966-80; RRID: AB_1210520
Rabbit monoclonal anti-p21 (167Er)	Cell Signaling Technology	Cat# 2947; RRID: AB_823586
Rabbit monoclonal anti-phospho-AKT Ser473 (168Er)	Cell Signaling Technology	Cat# 4060; RRID: AB_2315049
Rabbit monoclonal anti-phospho-STAT3 Tyr705 (169Tm)	Cell Signaling Technology	Cat# 9145; RRID: AB_2491009
Rabbit monoclonal anti-EGFR (170Er)	Cell Signaling Technology	Cat# 4267; RRID: AB_2246311
Rabbit monoclonal anti-phospho-SMAD2 Ser465/467/ Smad3 Ser423/425 (171Yb)	Cell Signaling Technology	Cat# 8828; RRID: AB_2631089
Rabbit monoclonal anti-ERα (172Yb)	Cell Signaling Technology	Cat# 13258; RRID: AB_2632959
Rat monoclonal anti-CD49f (173Yb)	Biolegend	Cat# 313602; RRID: AB_345296
Rabbit monoclonal anti-phospho-STAT5 Tyr694 (174Yb)	Cell Signaling Technology	Cat# 4322; RRID: AB_10548756
Rabbit monoclonal anti-phospho-S6 Ser235/236 (175Lu)	Cell Signaling Technology	Cat# 4858; RRID: AB_916156
Mouse monoclonal anti-CK8/18 (176Yb)	Cell Signaling Technology	Cat# 4546; RRID: AB_2134843
Chemicals, Peptides, and Recombinant Proteins		
C49 (NCGC00371442)	This paper; Johansson et al. (2016)	N/A
C70 (NCGC00371443)	This paper; Johansson et al. (2016)	N/A
C48	Genentech	N/A
Fulvestrant	Sigma-Aldrich	I4409
4-hydroxytamoxifen	Sigma-Aldrich	T176
β-Estradiol	Sigma-Aldrich	E2758
GSK126	Selleckchem	Cat# S7061
Critical Commercial Assays		
CellTiter-Glo Luminescent Cell Viability Assay	Promega	G7573
ThruPLEX DNA-seq 48S Kit	RUBICON	R400427
Deposited Data		
All raw genomic data	GEO	GSE104988
Experimental Models: Cell Lines		
MCF7 cells	Marc Lippman (University of Michigan)	N/A
T-47D cells	ATCC	HTB-133
ZR-75-1 cells	ATCC	CRL-1500
BT-474 cells	ATCC	HTB-20
SUM185 cells	Steve Ethier (University of Michigan)	N/A
SUM159 cells	Steve Ethier (University of Michigan)	N/A
SUM 149 cells	Steve Ethier (University of Michigan)	N/A
MDA-MB-231 cells	ATCC	HTB-26
BT549 cells	ATCC	HTB-122
HCC1937 cells	ATCC	CRL-2336
HCC2157 cells	ATCC	CRL-2340
KDM5-C49R	This paper	N/A
KDM5-C70R	This paper	N/A
FULVR	This paper	N/A
TAMR	This paper	N/A
MCF7-*ESR1*^{Y537S}	Myles Brown	N/A
MCF7 sgcontrol cells	This paper	N/A
MCF7 *KDM5B*-KO#1 cells	This paper	N/A
MCF7 *KDM5B*-KO#2 cells	This paper	N/A
MCF7 *KDM5A*-KO#1 cells	This paper	N/A
MCF7 *KDM5A*-KO#2 cells	This paper	N/A

(*Continued on next page*)

Continued

REAGENT or RESOURCE	SOURCE	IDENTIFIER
Recombinant DNA		
Edit-R Lentiviral Blast-Cas9	Dharmacon	CAS10138
Edit-R Lentiviral sgRNA Non-targeting Control	Dharmacon	GSG11812
Edit-R Human KDM5B Lentiviral sgRNA#1	Dharmacon	GSGH11838-246552182
Edit-R Human KDM5B Lentiviral sgRNA#2	Dharmacon	GSGH11838-246552189
Edit-R Human KDM5A Lentiviral sgRNA#1	Dharmacon	GSGH11838-246592353
Edit-R Human KDM5A Lentiviral sgRNA#2	Dharmacon	GSGH11838-246592357
Oligonucleotides		
ON-TARGETplus Non-targeting siRNA#1	Dharmacon	D-001810-03-05
ON-TARGETplus Non-targeting siRNA#2	Dharmacon	D-001810-04-05
ON-TARGETplus Human ESR1 siRNA#1	Dharmacon	J-003401-11
ON-TARGETplus Human ESR1 siRNA#2	Dharmacon	J-003401-12
ON-TARGETplus Human ESR1 siRNA#3	Dharmacon	J-003401-13

CONTACT FOR REAGENT AND RESOURCE SHARING

Further information and requests for resources and reagents should be directed to and will be fulfilled by the Lead Contact, Kornelia Polyak, Dana-Farber Cancer Institute, 450 Brookline Ave., Boston, MA 02215, USA. E-mail: kornelia_polyak@dfci.harvard.edu; tel: 617-632-2106; fax: 617-582-8490.

EXPERIMENTAL MODEL AND SUBJECT DETAILS

Breast Cancer Cohort Data

We obtained the normalized gene counts, isoform counts and exon counts data (Level 3, RNAseqV2) and clinical data from The Cancer Genome Atlas (TCGA) Broad GDAC Firehose database (https://gdac.broadinstitute.org/). Normalized microarray gene expression and clinical data of a cohort of 132 primary tumors from tamoxifen-treated patients followed up more than 5-years were obtained from GEO accession number GSE9893 (Chanrion et al., 2008). We also analyzed an unpublished dataset of RNA-seq gene expression RPKM (Reads Per Kilobase of transcript, per Million mapped reads) of a cohort of 109 ER^+ distant metastases that are part of the Metastatic Breast Cancer Project (Cohen et al., 2017). Breast cancer patients were >18 years of age and all but one female. Informed consent was obtained from all patients and the study was approved by the Dana-Farber/Harvard Cancer Center Institutional Review Board (DF/HCC Protocol 05-246).

Breast Cancer Cell Lines

Breast cancer cell lines were obtained from ATCC or generously provided by Steve Ethier (SUM cell lines, University of Michigan) and Marc Lippman (MCF7 cells, University of Michigan) and cultured following the provider's recommendations. Briefly, MCF7, C70R and C49R cells were cultured in DMEM supplemented with 10% FBS, 1% penicillin/streptomycin and 10 μg/ml insulin. FULVR, TAMR, and MCF7 as their corresponding control were cultured in RPMI without phenol red supplemented with 10% charcoal-stripped FBS, 1% penicillin/streptomycin and 10 μg/ml insulin. For estrogen deprivation/stimulation experiments cells were cultured in RPMI without phenol red supplemented with 10% charcoal-stripped FBS, 1% penicillin/streptomycin. Fulvestrant-resistant cells were generated by culturing parental MCF7 cells in phenol red-free RPMI containing 10% charcoal stripped FBS over a period of 3 months in the presence of 10μM fulvestrant, and then maintained them in 1μM fulvestrant.

Barcoding and Selection for Resistant Cells

High-complexity barcode library, ClonTracer, was as a kind gift from Frank Stegmeier (Novartis). Barcoding experiments were performed as previously described. Briefly, MCF7 cells were barcoded by lentiviral infection using 8 μg/ml polybrene. After a 24 h incubation with virus, infected cells were selected with 2 μg/ml puromycin. To ensure that the majority of cells were labeled with a single barcode per cell, for lentiviral infection we used a target m.o.i. of approximately 0.2, corresponding to 20% infectivity after puromycin selection. Infected cell populations were expanded in culture for the minimal time period to obtain a sufficient number of cells to set up replicate experiments. Barcoded MCF7 cells were treated with four different inhibitors: fulvestrant (10 μM), 4-OHT (5 μM), KDM5-C70 (10 μM) and KDM5-C49 (10 μM). The control groups were treated with 0.1% DMSO. Each group was cultured in quadruplicate. Cells were cultured in DMEM supplemented with 10% FBS, 1% penicillin/streptomycin and 10 μg/ml insulin for KDM5-C70, KDM5-C49 and their corresponding control or RPMI without phenol red supplemented with 10% charcoal-stripped FBS, 1% penicillin/streptomycin and 10 μg/ml insulin for fulvestrant, 4-OHT and their corresponding control. To keep the baseline control population as close as possible to that of the treatment group, each treatment group was cultured at the same passage as their

corresponding control group, because random barcode loss during passaging has been reported previously. Genomic DNA was extracted from the frozen cell populations with a QIAamp DNA Mini Kit (Qiagen). We used PCR to amplify the barcode sequence for NGS by introducing Illumina adaptors and 5-bp-long index sequences. Uniquely indexed libraries were pooled in equimolar ratios and sequenced on an Illumina NextSeq500 with single-end 75 bp reads by the Dana-Farber Cancer Institute Molecular Biology Core Facilities.

Animal Model

For xenograft assays female NOD.Cg-Prkdc^{scid} Il2rg^{tm1Wjl}/SzJ mice at 5–6-weeks of age were purchased from the Jackson Laboratory. Animal experiments were performed by the Lurie Family Imaging Center following protocols approved by the Dana-Farber Cancer Institute Animal Care and Use Committee.

METHOD DETAILS

Cellular Viability Assay

Cellular viability assays (N = 6) were performed using CellTiter-Glo (Promega) ten days after treatments and repeated 2–3 times. Cells were plated in 96-well plates and treated with inhibitors. Cells were cultured at 37°C with 5% CO, and the medium was replaced with fresh medium (with or without inhibitors) every two days.

ChIP-seq and RNA-seq

For KDM5B ChIP-seq, 1 × 10^7 cells were fixed with 2mM DSG (Thermo Fisher Scientific cat#20593) for 30 min at room temperature. DSG was then removed and replaced with fixing buffer (50 mM HEPES-NaOH (pH 7.5), 100 mM NaCl, 1 mM EDTA) containing 1% paraformaldehyde (Electron Microscopy Sciences, 15714) and crosslinked for 10 min at 37°C. For histone modification ChIP-seq, 5 × 10^6 cells were fixed with 1% paraformaldehyde for 10 min at room temperature. For ER ChIP-seq, 1 × 10^7 cells were fixed with 1% paraformaldehyde for 10 min at 37°C. Crosslinking was quenched by adding glycine to a final concentration of 0.125 M. Cells were washed with ice-cold PBS and harvested in PBS. The nuclear fraction was extracted by first resuspending the pellet in 1 ml of lysis buffer (50 mM HEPES-NaOH (pH 8.0), 140 mM NaCl, 1mM EDTA, 10% glycerol, 0.5% NP-40, and 0.25% Triton X-100) for 10 min at 4°C. Cells were pelleted, and washed in 1 ml of wash buffer (10 mM Tris-HCL (pH 8.0), 200 mM NaCl, 1 mM EDTA) for 10 min at 4°C. Cells were then pelleted and resuspended in 1 ml of shearing buffer (10 mM Tris-HCl (pH 8), 1 mM EDTA, 0.1% SDS) and sonicated in a Covaris sonicator. Lysate was centrifuged for 5 min at 14,000 rpm to purify the debris. Then 100 μl of 10% Triton X-100 and 30 μl of 5M NaCl were added. The sample was then incubated with 20 μl of Dynabeads Protein G (LifeTechnologies,10003D) for 1 h at 4°C. Primary antibodies were added to each tube and immunoprecipitation (IP) was conducted overnight in the cold room. Cross-linked complexes were precipitated with Dynabeads Protein G for 2 hr at 4°C. The beads were then washed in low salt wash buffer (20 mM Tris-HCl pH 8, 150 mM NaCl, 10 mM EDTA, and 1% SDS) for 5 min at 4°C, high salt wash buffer (50 mM Tris-HCl pH 8, 10 mM EDTA, and 1% SDS) for 5 min at 4°C and LiCl wash buffer (50 mM Tris-HCl pH 8, 10 mM EDTA, and 1% SDS) for 5 min at 4°C. DNA was eluted in elution buffer (100 mM sodium bicarbonate and 1% SDS). Cross-links were reversed overnight at 65°C. RNA and protein were digested with 0.2 mg/ml RNase A for 30 min at 37°C followed by 0.2 mg/ml Proteinase K for 1 h at 55°C. DNA was purified with phenol-chloroform extraction and isopropanol precipitation. ChIP-seq libraries were prepared using the Rubicon ThruPLEX DNA-seq Kit from 1 ng of purified ChIP DNA or input DNA according to the manufacturer's protocol. RNA-seq: Total RNA was extracted using the RNeasy Mini Kit (Qiagen). RNA-seq libraries were prepared using Illumina TruSeq Stranded mRNA sample preparation kits from 500 ng of purified total RNA according to the manufacturer's protocol. The finished dsDNA libraries were quantified by Qubit fluorometer, Agilent TapeStation 2200, and RT-qPCR using the Kapa Biosystems library quantification kit according to manufacturer's protocols. Uniquely indexed libraries were pooled in equimolar ratios and sequenced on an Illumina NextSeq500 with single-end 75 bp reads in the Dana-Farber Cancer Institute Molecular Biology Core Facilities.

Xenograft Assays

For xenograft assays 5–6-weeks old female NOD.Cg-Prkdc^{scid} Il2rg^{tm1Wjl}/SzJ mice were purchased from The Jackson Laboratory. Twenty-four hours prior to implantation of MCF7 cells, estrogen pellets (0.18 mg/pellet 17β-estradiol, 90-day release, Innovative Research of America) were implanted subcutaneously between the scapulae of mice. Tumors were induced by bilateral orthotopic mammary fat pad injection of 5 × 10^6 cells suspended in 100 μl of culture medium/Matrigel Growth Factor Reduced Basement Membrane Matrix, Phenol Red-Free (Corning) in a 1:1 ratio. Animal experiments were performed by the Lurie Family Imaging Center following protocols approved by the Dana-Farber Cancer Institute Animal Care and Use Committee. After 27 days, mice were randomized to treatment groups based on tumor size. Mice were administered FULV (5 mg per dose, weekly), KDM5 inhibitor 48 (100 mg per kg, BID), combination of FULV and 48, or vehicle only (control) for 21 days. Tumors implanted in mice were imaged using magnetic resonance imaging (MRI). Mice were euthanized and tumors collected 22 days after injection.

Immunoblotting

Cells were lysed in RIPA buffer. Proteins were resolved in SDS-polyacrylamide gels (4–12%) and transferred to PVDF membranes by using a Tris-glycine buffer system. Membranes were blocked with 2.5% milk powder in 0.1% Tween20 in TBS (TBS-T) for 1 h at room

temperature followed by incubation with primary antibodies in 2.5% milk TBS-T. The membranes were developed with Immobilon substrate (EMD Millipore).

Immunofluorescence Analyses

After deparaffinization and rehydration, slides were subjected to antigen retrieval in citrate buffer (pH 6; Dako) for 20 min in a steamer. Blocking solution (100% goat serum) was applied for 10 min. Incubation with primary antibody in PBS with 5% goat serum was held overnight at 4°C in a moist chamber. Secondary antibody was applied for 1 h at room temperature. Samples were mounted with VectaShield HardSet Antifade Mounting Medium with DAPI (Vector Laboratories). Imaging was performed in Servicebio (http://www.servicebio.com).

Antibodies and Inhibitors

Compounds KDM5-C49 and KDM5-C70 were synthesized following the reported procedure (Tumber et al., 2017), and also sourced from commercial vendors. All the chemical reagents and anhydrous solvents were purchased from Sigma-Aldrich and Strem. Preparative purification was performed on a Waters semi-preparative HPLC system using a Phenomenex Luna C18 column (5 micron, 30 x 75 mm) at a flow rate of 45 mL/min. The mobile phase consisted of acetonitrile and water (each containing 0.1% trifluoroacetic acid). A gradient of 10% to 50% acetonitrile over 8 min was used during the purification. Fraction collection was triggered by UV detection (220 nm). Analytical analysis was performed on an Agilent LC/MS (Agilent Technologies, Santa Clara, CA). A 7 min gradient of 4% to 100% Acetonitrile (containing 0.025% trifluoroacetic acid) in water (containing 0.05% trifluoroacetic acid) was used with an 8 min run or a 3 min gradient of 4% to 100% Acetonitrile (containing 0.025% trifluoroacetic acid) in water (containing 0.05% trifluoroacetic acid) was used with a 4.5 min run time at a flow rate of 1 mL/min. Phenomenex Luna C18 column (3 micron, 3 x 75 mm) or Phenomenex Gemini Phenyl column (3 micron, 3 x 100 mm) was used at a temperature of 50°C. Purity determination was performed using an Agilent Diode Array Detector. Mass determination was performed using an Agilent 6130 mass spectrometer with electrospray ionization in the positive mode. 1H NMR spectra were recorded on Varian 400 MHz spectrometers. Chemical shifts are reported in ppm with undeuterated solvent (DMSO-d6 at 2.49 ppm) as internal standard for DMSO-d6 solutions. All of the analogs tested in the biological assays have purity greater than 95%, based on both analytical methods. High resolution mass spectrometry was recorded on Agilent 6210 Time-of-Flight LC/MS system. Confirmation of molecular formula was accomplished using electrospray ionization in the positive mode with the Agilent Masshunter software (version B.02). Fulvestrant (I4409), 4-hydroxytamoxifen (4-OHT, T176) and β-Estradiol (E2758) were from Sigma, GSK126 was purchased from Sellechem, and KDM5 inhibitor 48 was provided by Genentech under a Material Transfer Agreement. Antibodies used for immunoblotting were anti-KDM5B (Sigma, HPA027179), anti-H3K4me3 (Abcam, ab1012), anti-H3K4me2 (Millipore, 07-030), anti-H3K4me1 (Abcam, ab8895), and anti-Histone H3 (Abcam, ab1791), β actin (Sigma, A2228), anti-H3K27Ac (Abcam, ab4729), anti-H3K27me3 (Abcam, ab6002), anti-H3K27me2 (Abcam, ab24684), anti-H3K36me2 (Abcam, ab9049), anti-H3K9Ac (Abcam, ab4441), anti-H3K79me2 (Abcam, ab3594), anti-SUZ12 (Cell Signaling, 3737), anti-EZH2 (Cell signaling, 5246), anti-ERα (Cell Signaling, 8644) , anti-phospho-ERα Ser118 (Cell Signaling, 2511). The antibodies used for ChIP were anti-KDM5B (Novus Biologicals, 22260002), anti-H3K4me3 (Abcam, ab1012), anti-H3K4me2 (Millipore, 07-030) and anti-ERα (Cell Signaling, 8644). Antibodies used for Immunofluorescence were anti-Cleaved Caspase-3 (Cell Signaling, 9661; 1:200 dilution), anti-Histone H3 phospho S10 (Abcam, ab5176; 1:200 dilution), anti-H3K4me3 (Abcam, ab8580; 1:500 dilution) and goat anti-rabbit IgG (H+L) conjugated to Alexa Fluor 488 (Thermo Fisher Scientific; 1:100 dilution).

CRISPR Experiments

Lentiviral Blast-Cas9, lentiviral sgRNA non-targeting control, KDM5B lentiviral sgRNA and KDM5A lentiviral sgRNA were purchased from Dharmacon. Following selection with blasticidin for Cas9, MCF7 cells were infected with each sgRNA and selected with puromycin. Knockout efficacy was determined by western blotting and cells were seeded for cell viability assays as described above.

inDrop

8×10^4 cells were pelleted and resuspended in 1 ml of 15% OptiPrep Density Gradient Medium (Sigma). Single-cell RNA-seq was performed using the inDrop protocol on a custom system as described (Zilionis et al., 2017). Hydrogel beads with version 3 oligonucleotide design were purchased from the Harvard Single Cell Core (https://iccb.med.harvard.edu/single-cell-core). Microfluidic encapsulation chips were purchased from 1CellBio (part no. 10080). Library preparation was performed as described (Zilionis et al., 2017).

Mass Cytometry

Antibodies used for mass cytometry in this study are listed in a table above. All antibodies were purchased in carrier-free buffers from the indicated sources and conjugated with the respective lanthanide metals by the CyTOF Antibody Resource and Core at Brigham Women's Hospital, Boston, MA, USA. Cells were treated with 50 μM IdU-127 (Fluidigm, South San Francisco, CA, USA) for 30 min and 100 μM of the intercalator-103Rh (Fluidigm) for 15 min at 37°C in their respective medium. Next, $1x10^6$ cells of each sample were barcoded using the Cell-ID 20-Plex Pd Barcoding Kit (Fluidigm) according to the manufacturer's instructions. Barcoded samples were pooled and stained simultaneously. Cells were fixed for 10 min with paraformaldehyde (Electron Microscopy Sciences, Hattfield, PA, USA) at a final concentration of 1.6 % followed by Fc-receptor block (Human TruStain FcX, Biolegend, San Diego,

CA) for 10 min and surface antibody staining for 30 min at room temperature. Subsequently, cells were permeabilized with methanol for 10 min on ice and incubated with the antibody cocktail for intracellular epitopes for 30 min. Cells were kept at 4°C overnight in Fix and Perm Buffer (Fluidigm) supplemented with Intercalator-IR (Fluidigm) 1:2000. Prior to analysis cells were washed with water, resuspended in water containing EQ™ Four Element Calibration Beads (Fluidigm) (1:10) and filtered through a 35 μm strainer. Samples were acquired at a CyTOF Helios instrument (Fluidigm), normalized as previously described (Bendall et al., 2011) and analyzed with Cytobank (Cytobank, Inc., Mountain View, CA). For all washes during staining Cell Staining Media (PBS with 0.5% BSA, 0.02% NaN3) was used.

Mass Spectrometry Analysis of Histone Modifications

Briefly, histones were isolated from cell nuclei using acid extraction, biochemically prepared, and analyzed by mass spectrometry against a reference of stable isotope-labeled synthetic peptide standards exactly as described (Creech et al., 2015).

QUANTIFICATION AND STATISTICAL ANALYSIS

ChIP-seq Analysis

Adapter sequences of ChIP-seq raw reads are removed by using cutadapt (https://doi.org/10.14806/ej.17.1.200). Trimmed reads are aligned by bowtie2 using default parameters to version hg19 of human genome. The samtools (Li et al., 2009) and picard (http://broadinstitute.github.io/picard) are used to sort and remove duplicated reads to avoid PCR bias from the sequencing process. Each group of libraries after the above pre-processing is down-sampled (without replacement) to a fixed number of reads. Peak calling (identification of regions of ChIP-seq enrichment over background) is performed by using MACS2 (Zhang et al., 2008) with parameters of "–extsize=146 –nomodel". The "broad peak" option is on when identifying binding regions of KDM5B, H3K4me3 and H3K4me2.

RNA-seq Analysis

Raw RNA-seq reads are aligned to version hg19 of human genome by using Tophat2 (Kim et al., 2013) with the default parameters. Gene counts are quantified by using HT-seq (Anders et al., 2015) with REFSEQ annotation. Differentially expressed genes are identified by using DEseq2 (Love et al., 2014) with cutoff of q value < 0.01 and fold change > 1.5, ranked by the statistics.

Barcoding Data Analysis

We followed the method used in Bhang et al., (2015) with small modifications. In details, all sequencing reads are trimmed by using 3' adaptor sequence: AGCAGAGCTACGCACTCTATGCTAGTGCTAGAGATCGGAAGAGCACACGTCTGAACTCCAGTCACTCACGAT CGTATCTCGTATGCCGTCTTCTGCTTG with minimum alignment length of 40-nt. The trimmed reads with Ns or less than 30-nt or without the WS x 15 pattern are removed. Then the 30-nt barcode sequences are extracted from the 3' prime end of the trimmed sequences. Barcodes with an estimated Phred quality score of at least 10 for all nucleotides and with an average Phred quality score greater than 30 are kept as qualified barcodes. The barcodes with only one count are excluded from the analyses to avoid the noise derived from the sequencing error.

Exome Sequencing

Exome sequencing was performed in the Dana-Farber Cancer Institute Center for Cancer Genome Discovery.

Library Preparation and Sequencing

Sequencing libraries were prepared as previously described (Brastianos et al., 2013). Briefly, gDNA from five cell lines and one human CEPH normal (http://hapmap.ncbi.nlm.nih.gov/citinghapmap.html.en) were fragmented to 250 bp using Adaptive Focused Acoustics (AFA) ultra-sonication (Covaris Inc., Woburn, MA) and further purified using Agencourt AMPure XP beads (Beckman Coulter, Inc., Indianapolis, IN). A total of 50 ng of size-selected DNA was ligated to DNA barcoded adaptors during library preparation (KAPA HTP DNA Library Preparation Kit, KK8234, Kapa Biosystems, Inc., Wilmington, MA). Each library was made with sample-specific barcodes and quantified using an Illumina MiSeq Nano flow cell (Illumina Inc., San Diego, CA). For exome enrichment, the 6 libraries were pooled in 3 x 2-plex to a total of 750 ng per pool, and exonic regions were captured with the SureSelect Target Enrichment system using the Human All Exon V5 hybrid capture kit (Agilent Technologies, Santa Clara, CA). All captures were further pooled and sequenced in two lanes of the HiSeq 2500 system in Rapid Run Mode (Illumina Inc., San Diego, CA).

Demultiplexing, Mapping, SNV, Indel and Copy Number Calling

Samples sequenced in the same lane were demultiplexed using the Picard tools. Read pairs were aligned to the hg19 reference sequence using the Burrows-Wheeler Aligner (Li and Durbin, 2009), and data were sorted and duplicate-marked using Picard tools. The alignments were further refined using the Genome Analysis Toolkit (GATK) (DePristo et al., 2011; McKenna et al., 2010) for localized realignment around indel sites (https://software.broadinstitute.org/gatk/documentation/tooldocs/current/org_broadinstitute_gatk_tools_walkers_indels_IndelRealigner.php). Recalibration of quality scores was also performed using the GATK (http://gatkforums.broadinstitute.org/discussion/44/base-quality-score-recalibration-bqsr). Mutation analysis for single nucleotide variants (SNV) was performed using MuTect v1.1.4 (Cibulskis et al., 2013) in paired mode using the CEPH as the "project normal," and indel calling was performed using the GATK SomaticIndelDetector tool. SNVs and indels were annotated using Variant Effect Predictor (McLaren et al., 2010). Copy number variants were identified using RobustCNV, an algorithm in development at the CCGD

(M. Ducar, personal communication). RobustCNV relies on localized changes in the mapping depth of sequenced reads to identify changes in copy number at the loci sampled during targeted capture. This strategy includes a normalization step in which systematic bias in mapping depth is reduced or removed using robust regression to fit the observed tumor mapping depth against a panel of normals (PoN) sampled with the same capture bait set. Observed values are then normalized against predicted values and expressed as log2ratios. A second normalization step is then done to remove GC bias using a loess fit. Finally, log2ratios are centered on segments determined to be diploid based on the allele fraction of heterozygous SNPs in the targeted panel. Normalized coverage data is next segmented using Circular Binary Segmentation (Olshen et al., 2004) with the DNAcopy Bioconductor package. Finally, segments are assigned "gain," "loss," or "normal-copy" calls using a cutoff derived from the within-segment standard deviation of post-normalized mapping depths and a tuning parameter which was set based on comparisons to array-CGH calls in separate validation experiments.

Resistant Cell-specific Mutations and Downstream GSEA Analysis

Resistant cell-specific mutations in each cell line were defined as mutations observed in that resistant cell line with variant allele frequency $\geq$ 10% and coverage $\geq$ 30, but not observed in parental MCF7 cell line. Downstream GSEA is a pathway-based algorithm. We searched seven available pathway databases (KEGG, BIOCARTA, REACTOME, NCI, SPIKE, HUMANCYC and PANTHER) to identified downstream genesets of each resistant-specific mutation. Then we used GSEA algorithm to calculate whether these downstream genesets are significantly differentially expressed between parental MCF7 and corresponding resistant cell line. The GSEA q value can thus represent the functional effect of each resistant cell-specific mutation.

List of Lentiviral Integration Sites in Drug-Resistant Single Clones

Clone Name	Insertion Site	Intergenic/Intronic/Exonic	Nearest Gene	Nearest Exon	Distance (bp)
bFULVR_1	Chr6: 111656384	Intronic	REV3L	Upstream of exon 23	441
bFULVR_2	Chr10: 5058744	Intronic	AKR1C2	Downstream of exon 1	1,348
bFULVR_3	Chr3: 167413258	Intronic	PDCD10	Downstream of exon 6	126
bFULVR_4	Chr3: 177415316	Intergenic	PROP1	Downstream of gene	3,920
bFULVR_5	Chr3: 5058744	Intronic	AKR1C2	Downstream of exon 1	1,348
bFULVR_6	Chr3: 167413258	Intronic	PDCD10	Downstream of exon 6	126
bTAMR_1	Chr22: 42268989	Intronic	SREBF2	Upstream of exon 5	813
bTAMR_2	Chr16: 90017249	Intronic	DEF8	Downstream of exon 2	1,203
bTAMR_3	Chr5: 60786357	Intronic	ZSWIM6	Upstream of exon 3	256
bTAMR_4	Chr16: 90017249	Intronic	DEF8	Downstream of exon 2	1,203
bTAMR_5	Chr17: 57650363	Intronic	DHX40	Upstream of exon 4	114
bTAMR_6	Chr19: 49751444	Intergenic	TRPM4	Downstream of gene	36,346
bTAMR_7	Chr5: 60786357	Intronic	ZSWIM6	Upstream of exon 3	256

Genetic Heterogeneity and Clonality Analysis of Cell Lines

The aligned files (bam) are prepared as described in "Exome sequencing" section. FACETS (Shen and Seshan, 2016) is used to estimate the absolute copy number, ploidy and tumor purity of parental and resistant cell lines from aligned files. The cancer cell fraction (CCF) of the mutations identified by MuTect2 (Van der Auwera et al., 2013) are then estimated based on the absolute copy number, ploidy, tumor purity and variant allele frequency (VAF) as previously described (Landau et al., 2013; Lohr et al., 2014; McGranahan et al., 2015). All mutations are classified as either clonal or subclonal according to the confidence interval of the CCF estimates. Mutations are defined as clonal if the 95% confidence interval overlapped 1 and subclonal otherwise, which is used in (McGranahan et al., 2015). Thus, the genetic heterogeneity/diversity of each cell line can be approximated by using the proportion of subclonal mutations to all mutations.

Transcriptomic Heterogeneity Estimation in Clinical Samples

To access the relationship between *KDM5B* expression level and transcriptomic heterogeneity in primary human breast tumors, we stratified patients into four groups with identical sample size based on the *KDM5B* expression level in ER^+ and ER^- tumors, respectively. We then calculated Shannon's equitability using gene, exon and junction level counts, respectively, within each patient to estimate the transcriptomic heterogeneity at different levels. The Shannon's equitability is a normalized version of Shannon's index, in which "0" represents no heterogeneity and "1" represents the highest heterogeneity. The Shannon's equitability was chosen here because the total number of population (genes) may vary for different samples. High Shannon's equitability represents higher transcriptomic heterogeneity. The same analysis was applied for other histone demethylases and housekeeping genes. Patient survival was compared between low and high transcriptome heterogeneity cases (cut by median of transcriptome heterogeneity across patients) in all patients, ER^+ patients and ER^- patients in TCGA dataset.

Width versus Height Analysis of Histone Marks

Promoter H3K4me3 and H3K4me2 peaks were compared in a panel of breast cancer cell lines before and after treatment with KDM5-C70. All peaks were ranked by their height (read counts at the summit) from low to high and divided into 20 groups. For each of the height group (represented by the mean value in x-axis), the mean and the interquartile range of the peak width in bp are calculated and plotted in y-axis.

inDrop Data Analysis

Preprocessing of the inDrop Data

Single-cell RNA-seq data generated by inDrop version 3 were processed using the indrops pipeline developed by the Klein laboratory (https://github.com/indrops/indrops, v.0.3.1.1, commit 7979ee8a212fcec5ba726a8ccf8b7b8fa9db52cf, using Python 2.7, Rsem 1.3.0, Bowtie 1.1.1, Samtools 1.3.1, JDK 1.8.0_45) (Zilionis et al., 2017). Default parameters were applied (for Bowtie, m: 200, n: 1, l:15, e: 80; for Trimmomatic, LEADING: "28", SLIDINGWINDOW: "4:20", MINLEN: "16"; for UMI quantification, m: 10, u: 1, d: 600, split-ambigs: False, min_non_polyA: 15; for low complexity filter, max_low_complexity_fraction: 0.50; for output: output_unaligned_reads_to_other_fastq: False, filter_alignments_to_softmasked_regions: False). Alignment was performed against cDNA from Ensembl GRCh38.85 release. Empty or unproductive droplets were filtered out based on the low abundance of reads per barcode, with a threshold set manually for each dataset after inspection of the barcode abundance distribution.

Filtering and Normalization of the inDrop Data

To get a reliable single cell transcriptome dataset, we exclude the cells with less than 1,000 genes expressed (UMI > 0), and exclude the genes if they meet both of the criteria: expressed in less than 5% of all single cells and less than 50% of single cells of the same type. The filtered data is then normalized by using scran (Lun et al., 2016) with deconvolution within each cell type followed by re-scaling across cell types by using parameter ‘‘clusters’’ in computeSumFactors function. This setting can largely avoid the influence of differentially expressed genes across cell types on the normalization accuracy (detail refers to scran paper). tSNE is performed on the normalized data to visualize the single cells in 2 dimensions by using the top 500 most variable genes. Cell cycle phases of all single cells are assigned by using cyclone function in scran package.

Cellular Transcriptomic Heterogeneity of Cell Lines Based on inDrop Data

Transcriptomic heterogeneity is accessed by calculating the pair-wised Euclidean distance between single cells of the same type. All possible pair-wised distances are obtained, and the mean values are compared between cell types. The Wilcoxon rank sum test was applied and p values were shown.

Identification of Pre-existing Resistant Cells from Single Cell Transcriptome

Cell identity signatures of MCF7, KDM5-C70 and C70R cells: For each of the three cell types, we compare the bulk gene expression of it (three replicates) with the other two cells together (three replicates each). We choose the top most 100 up-regulated and down-regulated genes as the (up and down) signatures of the cell type. Cell identity signatures of MCF7, fulvestrant-treated MCF7 and FULVR cells were obtained in the same way. Calculation of cell identity score: For each single cell, we calculated the average expression of each set of up signature genes minus the average expression of each set of down signature genes as the cell identity score. We carried out a bootstrap procedure to estimate the significance of the cell identity score. We randomly select 1,000 sets of up and down signatures with the same size of the original true signatures, generated the bootstrap distribution of the cell identity score, and calculated the bootstrap p value based on the distribution. We classified the single cells based on the bootstrap p valuecutoff of 5%. If a cell did not pass the test of any signature, it is annotated as unclassified. We observed that a few cells passed the test of two cell identity signatures, but no cell passed the three cell identity signatures. Hexagonal plots (Figure 4) were used to show the bootstrap classification of single cells in cell populations of MCF7, KDM5-C70 or fulvestrant-treated MCF7, and C70R and FULVR, in which cells showed clear identity (passed the 5% threshold) are positioned on the edge of the plot.

Genes with Differential Percentage of Expressing Cells

To test genes with differential percentage of expressing cells between two cell populations, all single cells are ranked and grouped in 10 groups by their sequencing depth to avoid its influence. For each gene, the proportion of cells expressing it is calculated for each group, and a weighted t-test is performed to access the significance of the difference between two cell populations. FDR is then calculated to correct the multiple testing.

Gene Set Enrichment Analysis (GSEA)

GSEA of H3K4me3 width increase in C70 was performed against the genes with increased percent of expressing cells in C70 for all genes or genes without expression change. H3K4me3 width changes were calculated as the average width changes across all six cell lines in Figure 2C. GSEA of H3K4me3 width increase in time course of C70 treatment was performed against the differentially expressed genes between corresponding treatment and parental cells in Figure S2D. GSEA of gene expression changes between endocrine-resistant cells and parental MCF7 cells was performed against top 500 up- or down-regulated genes between C70R and parental MCF7 cells in Figure 4C. GSEA of gene expression changes between KDM5 inhibitor resistant cells and parental MCF7 cells was performed against ER binding genes of different clusters in Figure S4H.

Simulation Methods

We construct a 2-type birth-death-mutation process model with passaging to estimate the initial proportion of cells with preexisting resistance (ρ) and mutation probability (μ). In the model, cells live for an exponentially-distributed amount of time before splitting into

two daughter cells according to their birth and death rates which are estimated from 12-day cell-viability assays with and without treatment for each treatment (see Estimation of parameters). Upon splitting, a drug-sensitive cell may beget one sensitive and one resistant with probability equal to the mutation probability, μ or two sensitive cells with probability $(1 - \mu)$. Resistant cells remain resistant.

For each combination of μ and ρ, the process begins with 1.46×10^6 initial uniquely barcoded ancestor cells with the proportion ρ as a starting resistant proportion and the rest $(1-\rho)$ are sensitive. We then simulate the process by beginning with a 14-day expansion phase simulated as a birth-death-mutation process for cells in DMSO to account for the initial barcode expansion. For each treatment, 5×10^6 cells are sampled from the population into each of 8 subpopulations (4 treatment and 4 DMSO) using multinomial sampling with weights equal to the number of cells present for each barcode. Each subpopulation then goes through a series of expansions (birth-death-mutation process) and passaging (multinomial sampling with a size of 5×10^6 and weights equal to the population sizes after expansion) according to the experimental passage schedules associated with each drug (see below). The final passage consists of a birth-death-mutation process expansion without a sampling step. 10 simulations are run for each treatment, pre-existing proportion, and mutation probability, and the results are fit to the experimental results in order to estimate the mutation rate and pre-existing proportion of resistant cells. The proportion of resistant barcodes present after the experiments and the ratio of barcodes shared among four replicates between the treatment and control group are determined for comparison to the data.

The multinomial distribution provides a fast approximation for the true multidimensional hypergeometric distribution which is acceptable since the initial number of barcodes post expansion is large and a small number (relative to the expanded population size) are sampled for plating.

Passage Schedule for Simulations

Group	Passage Times (in Days)
MCF7-pp15	6, 7, 8, 7, 6, 8, 7, 7, 6, 8, 6, 7, 7, 7, 8, 6, 8, 6, 8, 6
C70	6, 10, 12, 10, 11, 10, 11, 10, 10, 9, 9, 11, 10, 10, 11, 12, 12, 11, 12, 13
C49	6, 10, 12, 10, 11, 10, 11, 10, 10, 9, 9, 11, 10, 10, 11, 12, 12, 11, 12, 13
MCF7	13, 15, 14, 14, 14, 10
Fulvestrant	28, 31, 24, 22, 14
Tamoxifen	21, 84, 69, 49, 17

Estimation of Parameters for Simulation

For each drug and control group, growth rates are estimated using 12-day cell viability assays to get the following rates: growth rate of resistant cells in DMSO ($\lambda_{r,DMSO}$), growth rate of resistant cells in treatment ($\lambda_{r,TR}$), growth rate of sensitive cells in DMSO ($\lambda_{s,DMSO}$), and growth rate of sensitive cells in treatment ($\lambda_{s,TR}$).

The growth rates of resistant populations, λ_r, are determined by fitting the number of viable cells to a log-transformed linear regression from experimentally generated data from resistant cell-lines. The estimated slope gives our estimated growth rate (see below). We use the resistant growth rate along with the number of cells in the control 12-day growth assay containing and unknown mixture of resistant and sensitive cells in order to determine the growth rate of sensitive cells. Given a particular value of ρ, we assume the control population grows approximately on according to the following equation:

$$N(t) = \rho N(0)e^{\lambda_r t} + (1 - \rho)N(0)e^{\lambda_s t}$$

where $N(t)$ is the number of cells at time t. This equation assumes a low mutation probability since the experiments contain fewer cells and are ran over a shorter time period. We solve for the growth rates of the sensitive population, (λ_s) with and without each drug, and we use this value along with the resistant cell line growth rates to parameterize the model. We assume the death rate is the same throughout the experiments and determine the birth rate from $b = \lambda + d$. Changing the death rate had little effect on the results. These growth parameters are used to parameterize the simulations along with the growth rates estimated from data.

Growth Rates of Resistant Cell Lines

Group	Growth Rates in DMSO ($Days^{-1}$)	Growth Rates in Drug ($Days^{-1}$)
C70-resistant	0.313	0.299
C49 resistant	0.321	0.305
Fulvestrant-resistant	0.221	0.173
Tamoxifen-resistant	0.199	0.142

DATA AND SOFTWARE AVAILABILITY

All raw genomic data was deposited to GEO: GSE104988.

Update

Cancer Cell
Volume 35, Issue 2, 11 February 2019, Page 330–332

DOI: https://doi.org/10.1016/j.ccell.2019.01.012

CellPress

Cancer Cell
Correction

KDM5 Histone Demethylase Activity Links Cellular Transcriptomic Heterogeneity to Therapeutic Resistance

Kunihiko Hinohara, Hua-Jun Wu, Sébastien Vigneau, Thomas O. McDonald, Kyomi J. Igarashi, Kimiyo N. Yamamoto, Thomas Madsen, Anne Fassl, Shawn B. Egri, Malvina Papanastasiou, Lina Ding, Guillermo Peluffo, Ofir Cohen, Stephen C. Kales, Madhu Lal-Nag, Ganesha Rai, David J. Maloney, Ajit Jadhav, Anton Simeonov, Nikhil Wagle, Myles Brown, Alexander Meissner, Piotr Sicinski, Jacob D. Jaffe, Rinath Jeselsohn, Alexander A. Gimelbrant, Franziska Michor,* and Kornelia Polyak*

*Correspondence: michor@jimmy.harvard.edu (F.M.), kornelia_polyak@dfci.harvard.edu (K.P.)

https://doi.org/10.1016/j.ccell.2019.01.012

(Cancer Cell *34*, 939–953.e1-e9; December 10, 2018)

In the originally published version of this article, the legend for Figure 6G was accidentally mixed up, and the purple and gray section of the pie chart was incorrectly marked. The correct Figure 6G is now shown here and in the online version of the paper. The authors apologize for any confusion this error may have caused.

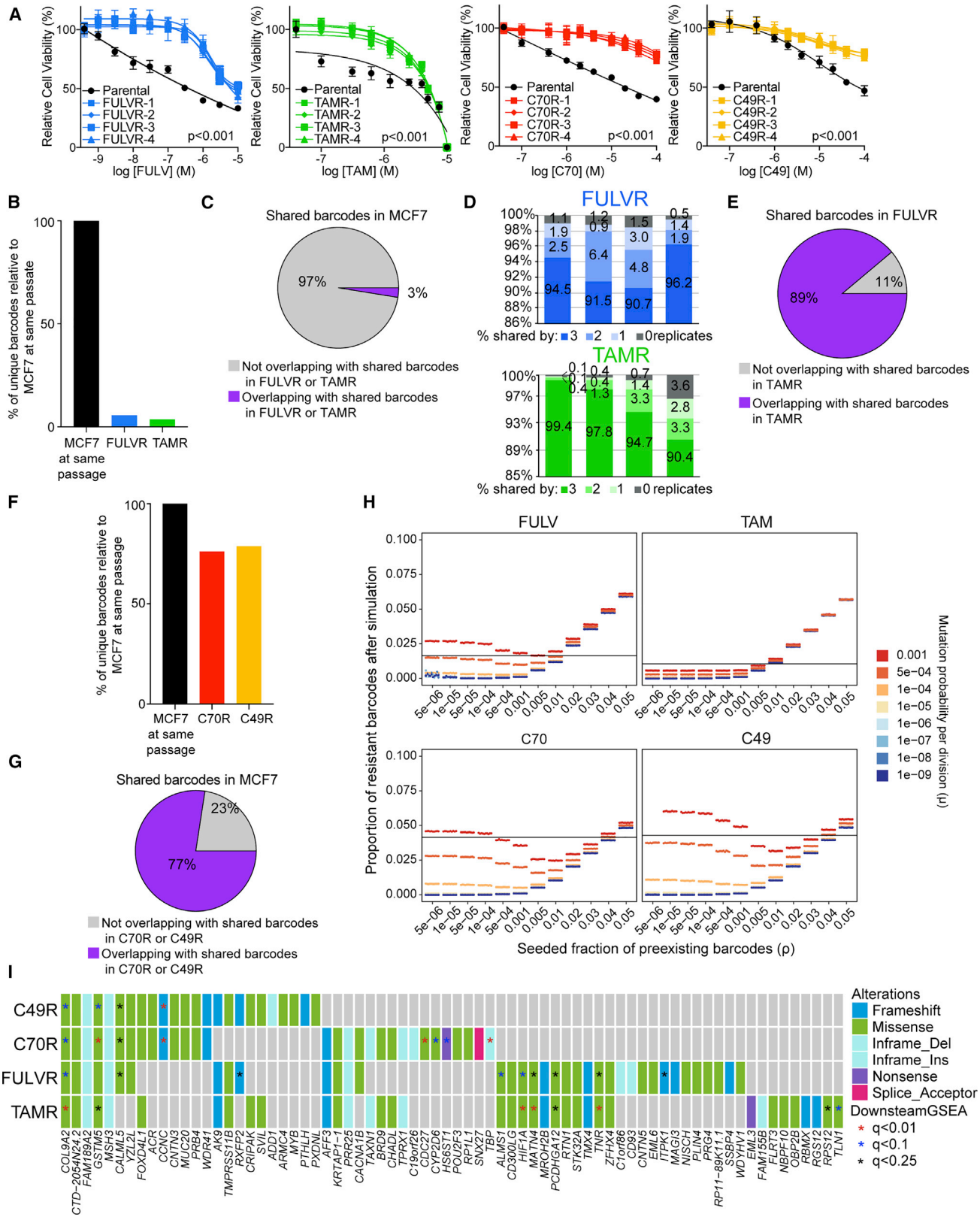

Figure 6. Resistance to Anti-estrogens and KDM5i in MCF7 Cells (corrected)

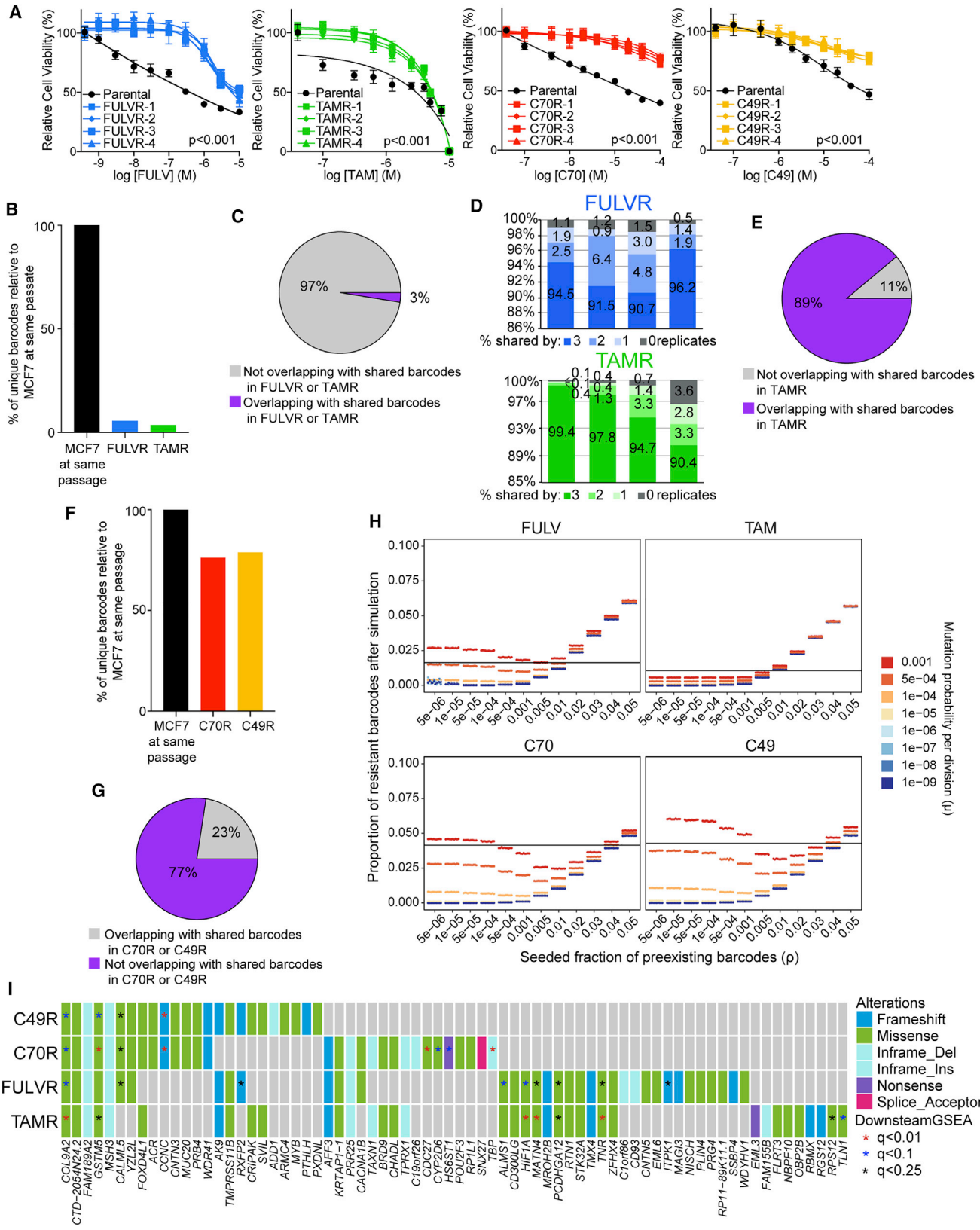

Figure 6. Resistance to Anti-estrogens and KDM5i in MCF7 Cells (original)